Applied Surface Science 660 (2024) 160028

Contents lists available at ScienceDirect

Applied Surface Science

journal homepage: www.elsevier.com/locate/apsusc

Full Length Article

Innovative ternary composite photocatalyst: $BiOCl/Bi_{12}O_{17}Cl_2/Bi_2O_3$ for sustainable water remediation

Helena Pérez del Pulgar [a], Josefa Ortiz-Bustos [a], Almudena Torres-Pardo [b], Marina Parras [b], Isabel del Hierro [a,*], Yolanda Pérez [a,c,*]

[a] COMET-NANO group, Departamento de Biología y Geología, Física y Química Inorgánica, ESCET, Universidad Rey Juan Carlos, C/ Tulipán s/n, 28933 Móstoles (Madrid), Spain
[b] Department of Inorganic Chemistry, Faculty of Chemical Sciences, University Complutense Madrid, 28040, Spain
[c] Advanced Porous Materials Unit, IMDEA Energy, Av. Ramón de la Sagra 3, 28935 Móstoles, Madrid, Spain

ARTICLE INFO

Keywords:
BiOCl-based ternary composite
Electrochemical properties
Visible light-active photocatalyst
Ciprofloxacin
Methyl paraben

ABSTRACT

The presence of pollutants in aquatic environments is causing severe health effects on both humans and animals. To address this issue, it has become crucial to develop more efficient and environmentally friendly photocatalysts for the removal of persistent pollutant mixtures from water. In this context, photocatalysts containing more than two bismuth-based materials have rarely been explored for water remediation. With this in mind, we propose an innovative ternary composite, $BiOCl\text{-}1/Bi_{12}O_{17}Cl_2/Bi_2O_3$, as a potentially sustainable visible light-active photocatalyst. Firstly, bismuth oxychloride has been prepared in the presence of ionic liquid, leading to the formation of BiOCl-1 with highly reactive {1 1 0} facets. Subsequently, the construction of the ternary composite has been accomplished using a facile and soft hydrothermal approach. The as-prepared $BiOCl\text{-}1/Bi_{12}O_{17}Cl_2/Bi_2O_3$ composite has been successfully used in degrading binary mixtures of contaminants (*i.e.* ciprofloxacin, methylparaben or methyl orange), achieving an improved visible-light photocatalytic activity compared to single BiOCl-1 and other previously reported bismuth-based photocatalysts. In addition, the photocatalytic mechanism and degradation pathways have been elucidated through scavenger and electrochemical experiments, as well as chromatography-mass spectrometry (LC-MS) analysis, respectively.

1. Introduction

Bismuth-based materials, such as bismuth oxyhalide (BiOX, X = Cl, Br, I), bismuth rich-bismuth oxyhalides ($Bi_xO_yX_z$), and bismuth oxide (Bi_2O_3), have garnered increasing attention. These materials have been recognized not only as encouraging photocatalysts (including environmental remediation, H_2 production, or CO_2 transformations) [1] but also as potential materials for biological applications [2]. This is due to their several favourable properties such as low toxicity, chemical stability, and cost-effectiveness. Besides, these materials exhibit excellent photocatalytic performances thanks to i) their 2D structure, which facilitates the separation of the electron-hole pairs ii) their narrow band gap, and iii) their highly stable photoactive sites. For instance, while BiOCl displays a limited visible photocatalytic activity by its large band gap (3.2 eV), $Bi_{12}O_{17}Cl_2$ and Bi_2O_3 are able to absorb visible light, with band gap values of around 2.1 and 2.5 eV, respectively, but resulting in fast recombination of photogenerated electrons and holes [3].

In this sense, several strategies have been developed to enhance the visible-active photocatalytic behaviour and promote the separation of photogenerated electrons-holes in bismuth-based photocatalysts, including ion doping, assembling heterojunctions, controlling morphology with modifiers or creating oxygen vacancies [4]. Specially, the formation of heterojunctions by coupling semiconductors has demonstrated to be a successful strategy for enhancing the photocatalytic performance of individual semiconductors. This strategy promotes electron-hole separation while intensifying the internal electrostatic field [5]. Thus, the photocatalytic ability of a heterojunction depends on factors such as the intimate contact of the semiconductors and their energy band positions [6]. The most commonly used heterojunctions consist of two components (binary composites), while configurations involving the combination of three or four components (ternary or quaternary composites) are used less frequently. Binary composites containing BiOCl have been successfully fabricated (e.g. $BiOCl/g\text{-}C_3N_4$ [7], $BaFe_2O_4/BiOCl$ [8], and $BiOCl/Ti_3C_2Tx$ Mxene

---

* Corresponding authors.
E-mail addresses: isabel.hierro@urjc.es (I. del Hierro), yolanda.cortes@urjc.es (Y. Pérez).

https://doi.org/10.1016/j.apsusc.2024.160028
Received 14 December 2023; Received in revised form 26 February 2024; Accepted 31 March 2024

[9]), including those composed of two bismuth-based components (e.g. $BiVO_4/BiOCl$ [9], $Bi_2O_3/BiOCl$ [10], $Bi_2O_2CO_3/BiOCl$ [11], $BiPO_4/BiOCl$ [12]), performing an improved visible light photodegradation activity. It is worth noting that co-sharing the Bi atom can boost the intimate contact between both components, facilitating the interfacial charge transfer [13]. For example, $Bi_{12}O_{17}Cl_2/\beta\text{-}Bi_2O_3$ composites, featuring great contact interfaces, were prepared by a solvothermal-calcining approach for degrading 4-tert-butylphenol [14]. Qiao et al. [15] prepared a highly efficient $Bi_{12}O_{17}Cl_2/BiOCl\text{-}O_V$ photocatalyst, gaining intimate contact between both components and the presence of oxygen vacancies. The combination of Bi_2O_3 and BiOCl [10] also achieved high photocatalytic performance for visible light degradation of bisphenol A and methylene blue, owing to the fast generation of an interface electric field and high electron migration (*i.e.* charge transfers resistance (R_{ct}) = 114, 523 and 889 Ω for $Bi_2O_3/BiOCl$, Bi_2O_3 and BiOCl photocatalysts, respectively). To date, photocatalysts composed of three bismuth-based components have been hardly reported (e.g. $BiOCl/(BiO)_2CO_3/Bi_2O_3$ [16] and $BiOI/Bi_4O_5I_2/Bi_2O_2CO_3$ [17]).

For the first time, we have successfully fabricated a novel ternary composite, $BiOCl\text{-}1/Bi_{12}O_{17}Cl_2/Bi_2O_3$. This composite contains robust BiOCl-1 with highly reactive {1 1 0} facets, as well as $Bi_{12}O_{17}Cl_2$ and $\beta\text{-}Bi_2O_3$ both of which possess excellent potential for absorbing visible-light and promoting photooxidations [18]. Furthermore, $Bi_{12}O_{17}Cl_2$ can produce hydroxyl radicals under visible light irradiation [19], enhancing the photodegradation process. The ternary composite is expected to combine the advantages of its individual components and compensate for their deficiencies. As a result, $BiOCl\text{-}1/Bi_{12}O_{17}Cl_2/Bi_2O_3$ exhibited an excellent ability in degrading and/or adsorbing a mixture of common contaminants present in wastewater such as ciprofloxacin (CIP) [20], methylparaben (MP) [21] and methyl orange (MO) [22]. Additionally, an in-depth characterization study has been conducted using HRTEM, XPS, and electrochemical analysis to i) validate the formation of the heterojunction, ii) assess charge transfer efficiency and iii) propose the photocatalytic mechanism.

2. Experimental section

2.1. Materials

Bismuth (III) nitrate pentahydrate ≥ 98 % ($Bi(NO_3)_3\ 5H_2O$) was acquired from Chem Lab and $\beta\text{-}Bi_2O_3$ from TODINI and CO. SPA. Sodium bismuth oxide 80 % ($NaBiO_3$) was purchased from Alfa Aesar and 1-butyl-3-metylimidazolium chloride > 98 % from Acros Organics. Ethylene glycol was purchased from Glentham Life Sciences and absolute ethanol from VWR Chemical. Water filtered by a Millipore Milli-Q system (Waters, USA) was used for all the experiments. Ciprofloxacin (CIP), methyl orange (MO) and methyl paraben (MP) were purchased from Merck, Acros Organics and Scharlab, respectively. Humic acid (HA), and sodium bicarbonate ($NaHCO_3$) were purchased from Sigma Aldrich and Scharlab respectively.

2.2. Synthesis of BiOCl samples

BiOCl samples were prepared according to the reported method with some slight modifications [23]. In a typical synthesis, 6 mmol of $Bi(NO_3)_3\ 5H_2O$ was dissolved in 44 mL ethylene glycol (EG) forming the solution A. Also, 6 mmol of potassium chloride and/or 1-butyl-3-metylimidazolium chloride were dissolved in 44 mL of water and added dropwise to solution A under magnetic agitation. Then, the mixture was stirred for 3.5 h at room temperature. The resulting white solid was filtered, washed with water and ethanol, and dried for 5 h at 70 °C. BiOCl materials, denoted as BiOCl-0, BiOCl-0.5, and BiOCl-1, were obtained using a molar ratio of 1-butyl-3-metylimidazolium chloride: KCl equal to 0:1, 0.5:0.5 and 1:0, respectively.

2.3. Synthesis of $BiOCl\text{-}1/Bi_{12}O_{17}Cl_2/Bi_2O_3$ ternary composite

1 g of BiOCl-1 was dispersed in 80 mL of water (solution A) and 0.5 g of $NaBiO_3$ was dispersed in 40 mL of water (solution B). Both solutions (A and B) were mixed and dispersed in an ultrasonic bath for 20 min. Then, the resulting dispersion was transferred into a 200 mL Teflon-lined stainless-steel autoclave for a hydrothermal reaction at 120 °C for 8 h. The resulting solid was washed with water and dried at 70 °C for 5 h. The resulting ternary composite was labelled as $BiOCl\text{-}1/Bi_{12}O_{17}Cl_2/Bi_2O_3$. For comparative purposes, $Bi_{12}O_{17}Cl_2$ was prepared following to previously reported method [24] and the commercial $\beta\text{-}Bi_2O_3$ material was acquired from TODINI and CO. SPA.

2.4. Characterization

A Phillips Diffractometer model PW3040/00 X'Pert MPD/MRD at 45 KV and 40 mA, with Cu-Kα radiation (λ = 1.5418 Å) was used to obtain the X-Ray diffraction (XRD) patterns of the materials. N_2 adsorption–desorption isotherms were acquired using a Micromeritics TriStar 3000 analyser. FT-IR spectra were collected using a Perking-Elmer Spectrum Two equipped with an attenuated total reflectance (ATR) mode (in the region 4000 to 400 cm^{-1}). DRUV–vis spectra were measured with A Perkin Elmer 850 spectrophotometer in diffuse reflectance mode. Images of field-emission scanning electron microscopy (FESEM) were acquired with a JEOL (JSM 7900F) scanning microscope at an accelerating voltage of 10 kV. High resolution transmission electron microscopy (HRTEM), and Energy-dispersive X-ray (EDX) spectroscopy were carried out using a transmission electron microscope JEOLJEM300F equipped with an EDS (OXFORD INCA) spectrometer. For TEM observations, the samples were ultrasonically dispersed in ethanol and then transferred to carbon coated copper grids. Solid-state emission spectra were recorded using a Perkin-Elmer LS 55 fluorescence spectrometer with a Xe lamp at 350 nm excitation wavelength. The zeta potential measures of bismuth-based materials were performed in a PBS solution (0.1 mg mL^{-1}) at pH 7 and using a Nanoplus Zeta Potential from Micromeritics. Electrochemical studies were performed with a potentiostat/galvanostat Autolab PSGTAT302 with an impedance module using modified carbon paste electrodes (MCPE) as working electrodes. The MCPE was prepared by mixing graphite, nujol as a binder and the sample (35 mg of graphite and 3.5 mg of the sample). Ag/AgCl/KCl (3 M) was used as a reference electrode, a platinum rod as a counter electrode, and a Na_2SO_4 0.2 M aqueous solution as electrolyte. Electrochemical impedance spectroscopy (EIS) was conducted similarly, using a 0.1 M aqueous KOH solution as the electrolyte. EIS measurements were performed from 0.01 Hz to 100000 Hz under OCP conditions. Metrohm NOVA 2.1.6 software was used for the simulated circuit fit of the EIS data. Photocurrent experiments were performed using commercial glassy carbon electrodes. An ink, composed of the material and Ketjenblack carbon (10 % of active material), was prepared in a mixture of absolute ethanol, Milli-Q water (50 %), and 20 μL of Nafion. Then, this ink was drop-casted onto the electrodes and air-dried. The experiment spanned a total of 100 s, divided into three cycles of 10 s of darkness followed by 20 s of light exposure.

2.5. Photocatalytic degradation of contaminants

The photocatalytic activity of bismuth-based materials was evaluated in the degradation of single contaminants as well as binary mixtures of ciprofloxacin (CIP) and methyl orange (MO) or methylparaben (MP) and methyl orange (MO) in water. A 300 W Xe lamp with a cut-off filter (λ > 420) was employed as visible light source. In a typical experiment, 20 mL of an aqueous solution of a single contaminant or a binary mixture (CIP (15 ppm), MP (10 ppm), MO (13 ppm)) and 20 mg of the photocatalyst were mixed in a 20 mL flask tube. The pH of the solution (pH = 4 and 8) was adjusted by using aqueous solutions of H_2SO_4 (0.1 M) and NaOH (0.1 M). For the matrix effect experiments, the polluted water was prepared containing 1 mg/L of humic acid (HA) or 0.5 mM of sodium bicarbonate ($NaHCO_3$), and then, the resulting solutions were spiked with either CIP or MP. The dispersion was stirred in darkness for 30 min to reach the adsorption–desorption equilibrium of the contaminant on the photocatalyst surface. Then, the mixture was irradiated under visible light for set periods of time. An aliquot of the reaction was taken at different time intervals and analysed by UV–Vis spectroscopy. The concentration of CIP, MP, or MO was determined by monitoring the change in absorbance at 272, 256, and 466 nm, respectively.

2.6. *Photocatalytic degradation mechanism experiments*

The scavenger trapping experiments were carried out using benzoquinone (BQ), ascorbic acid (AA), and 2-propanol (IPA) to quench superoxide ($O_2^{\bullet -}$), positive holes (h^+), and hydroxyl radicals ($^{\bullet}OH$). The degradation test was carried out as the degradations previously described but adding the corresponding scavenger (BQ, AA, or IPA) 2 mM and measuring at 30 min of light exposure. The degradation products were identified using an Agilent 1260 Infinity II system (Agilent Technologies, Santa Clara, CA, USA). This system is equipped with a 1260 DAD HS PDA detector and an API-Electrospray Source, operating in positive ion mode. The mobile phase (linear gradient from 95 % of aqueous solution 0.1 % formic Acid(A): 5 % Methanol (B) (0–5 min) to 5 % A: 95 % B (5–10 min)) was delivered at a flow rate of 0.3 mL/min at 35 °C, employing an InfinityLab Poroshell 120 EC-C18 column (2.7 μm x 2.1 x 50 mm). The retention times were 4.40 and 5.04 min for CIP and MP, respectively.

3. Results and discussion

3.1. *Synthesis and characterization of bismuth-based materials*

Firstly, BiOCl samples were synthesized by a precipitation method, varying the molar ratio of ionic liquid:KCl (i.e. 0:1, 0.5:0.5, and 1:0), yielding the materials denoted as BiOCl-0, BiOCl-0.5, and BiOCl-1, respectively. The X-ray diffraction (XRD) patterns of BiOCl samples are shown in Fig. S1. The most intense peaks of the as-prepared BiOCl samples are located at 11.8°, 25.9°, 32.5°, 33.4°, 40.9°, 46.7°, 49.7°, 54.2°, 58.6°, which are in accordance with the (0 0 1), (1 0 1), (1 1 0), (1 0 2), (1 1 2), (2 0 0), (1 1 3), (2 1 1), (2 1 2) planes of tetragonal BiOCl (JCPDS 00–060-0294), respectively. It is important to highlight that the addition of the ionic liquid, as a chloride source, affects the intensity ratio of (1 1 0)/(1 0 2) facets, which increases with the higher amount of the ionic liquid (*i.e.* intensity ratio of (1 1 0)/(1 0 2) peaks are 1.43, 1.62, 1.88 for BiOCl-0, BiOCl-0.5, BiOCl-1, respectively). This result indicates a more substantial anisotropic growth along the (1 1 0) plane when the ionic liquid is employed instead of KCl [25]. In this regard, Yang et al. demonstrated that BiOCl with the (1 1 0) facet highly exposed produced free electrons easily, achieving a superior photoactivity in degrading rhodamine B [26]. Besides, according to the XRD analysis (from the peaks at 2θ = 25.9, 32.5, and 33.4°), the BiOCl samples prepared with ionic liquid (BiOCl-0.5 and BiOCl-1) possess a smaller crystalline size than that calculated for BiOCl-0 (Table 1). This confirms that the presence of the ionic liquid has a significant influence on the growth of the tetragonal BiOCl.

Table 1
Textural properties and band gap values of bismuth-based samples.

Material	S_{BET} (m^2. g^{-1})	V_p[a] (cm^3. g^{-1})	Crystallite size (nm)[c]	Band gap (eV)[d]
BiOCl-0	23.66	0.09	21.9	3.41
BiOCl-0.5	31.25	0.19	20.5	3.48
BiOCl-1	37.84	0.17	20.6	3.48
BiOCl-1/$Bi_{12}O_{17}Cl_2$/Bi_2O_3	20.81	–	–	2.16

[a] Total pore volume calculated by the BJH method from the adsorption branch of the N_2 isotherm.

[c] Determined by Scherrer's equation

[d] Calculated by the application of the Kubelka-Munk equation.

As mentioned above, BiOCl-1, with a high content of reactive {1 1 0} facets, could exhibit an enhanced photocatalytic activity. Via a screening involving BiOCl samples, we assessed their photocatalytic effectiveness in removing CIP from water (see Fig. 12). BiOCl-1 showed a higher removal efficiency of CIP (95.7 % in 60 min) compared to BiOCl-0 (80.9 %), proving that the reactive {1 1 0} facets play a role in the photodegradation process, without disregarding the effect of textural properties (Table 1).

According to the results, BiOCl-1 was selected and transformed to the ternary composite, BiOCl-1/$Bi_{12}O_{17}Cl_2$/Bi_2O_3, in the presence of $NaBiO_3$ by a simple hydrothermal method. Thus, the addition of $NaBiO_3$ made it possible to produce $[Bi_2O_2]^{2+}$ [10] and subsequently form $Bi_{12}O_{17}Cl_2$ and Bi_2O_3. The XRD pattern of BiOCl-1/Bi_2O_3/$Bi_{12}O_{17}Cl_2$ (Fig. 1) displays the peaks ascribed to the tetragonal BiOCl phase (JCPDS 00–006-0249), maintaining the higher intensity of the (1 1 0) peak in relation to the (1 0 2) peak intensity. Furthermore, additional reflections are observed at 29.4° and 30.3° corresponding to the (1 1 7) and (0012) planes of $Bi_{12}O_{17}Cl_2$ tetragonal (JCPDS 00–037-0702), respectively, and 27.8° and 55.3° associated to (2 0 1) and (2 1 3) crystal facets of β-Bi_2O_3 (JCPDS 00–027-050), respectively.

To gain more insight into the formation mechanism of the BiOCl-1/$Bi_{12}O_{17}Cl_2$/Bi_2O_3 material, both precursors (i.e. BiOCl-1 and $NaBiO_3$) were subjected to the same hydrothermal treatment separately. After the treatment, the XRD pattern of BiOCl-1 (Fig. S2a), show no change compared to the pristine material, indicating that $Bi_{12}O_{17}Cl_2$ is not formed by the thermal decomposition of BiOCl-1. In the case of $NaBiO_3$ (Fig. S2b), a partial hydrothermal decomposition process occurred towards the formation of Bi_2O_3 (JCPDS 027–0050), while some of the original $NaBiO_3$ remained. The formation of Bi_2O_3 can be explained to the highly instability of Bi(V) in the $NaBiO_3$, with its reduction potential of 2.03 V [27]. Based on these results, we propose that the formation of the Bi_2O_3 is due to the addition of $NaBiO_3$ and the presence of the BiOCl-1 promotes the complete decomposition of $NaBiO_3$, since the peaks associated to $NaBiO_3$ are not observed in the XRD of the ternary composite (Fig. S2c). Besides, $Bi_{12}O_{17}Cl_2$ may be formed from Bi_2O_3 and BiOCl-1 via a thermal process. In accordance with this, Kato et al. prepared $Bi_{12}O_{17}Cl_2$ by thermal treatment of a mixture of Bi_2O_3 and BiOCl [28].

It is well known that the textural properties of the materials are one of the key factors in the removal of contaminants by adsorption/

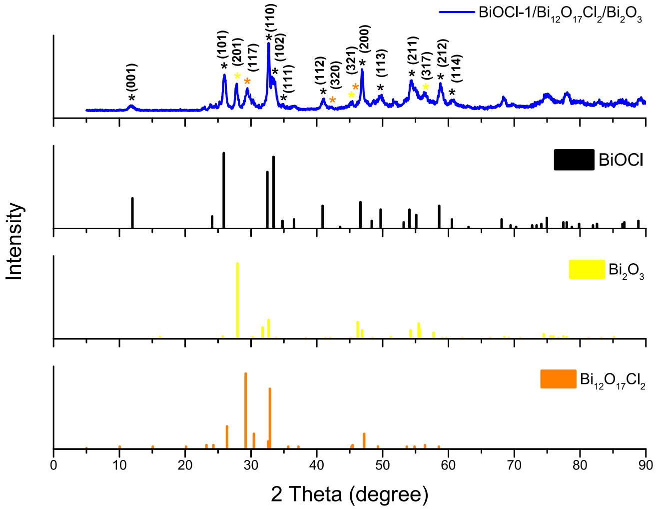

Fig. 1. Comparison of XRD patterns of BiOCl-1/$Bi_{12}O_{17}Cl_2$/Bi_2O_3 ternary composite and the standard samples.

photodegradation processes. Thus, adsorption–desorption isotherms of the as-prepared bismuth-based materials were obtained (Fig. S3). All samples exhibit a type IV of IUPAC classification with an H3 hysteresis, which indicates of the existence of porous from the aggregation of sheet-like particles [29]. As can be seen in Table 1, increasing the amount of ionic liquid, the specific surface area (S_{BET}) increases (from 23.66 to 37.84 m^2/g), as well as the pore volume (from 0.09 to 0.17 $cm^3\ g^{-1}$), suggesting that the addition of ionic liquid improves the textural properties of the material. In contrast, BiOCl-1/$Bi_{12}O_{17}Cl_2$/Bi_2O_3 composite shows type III BET isotherm, which can be attributed to the formation of slit-like pores [30]. The BET surface area of the ternary composite is slightly higher than those reported for composites such as BiOCl-$Bi_{12}O_{17}Cl_2$ [31] (20.81 vs 16.49 m^2/g).

The optical properties and charge separation of the bismuth-based materials were examined by UV–vis diffuse reflectance (DRUV–Vis) and photoluminescence spectroscopy, respectively. BiOCl samples mainly response to UV light, with an absorption edge around 365 nm (Fig. 2a). Clearly, BiOCl-1/$Bi_{12}O_{17}Cl_2$/Bi_2O_3 exhibits a red-shifted absorption edge compared with the single-materials, $Bi_{12}O_{17}Cl_2$, BiOCl and β-Bi_2O_3, indicating that the ternary composite can absorb visible light. The band gap values were calculated by applying the Kubelka-Munk function (Fig. 2b, Table 1). BiOCl samples possess similar band gap values around 3.4 eV, while a significant reduction in the band gap is observed upon the formation of the composite (from 3.4 to 2.16 eV). This observation infers the successful construction of the ternary heterojunction. In addition, the separation of photogenerated charge carriers for the bismuth-based materials was analysed by photoluminescence measurements (Fig. S4). Thus, the formation of the composite involves a remarkable reduction in the PL intensity, implying that BiOCl-1/$Bi_{12}O_{17}Cl_2$/Bi_2O_3 composite leads to a better separation of electron–hole pairs compared to the individual BiOCl samples.

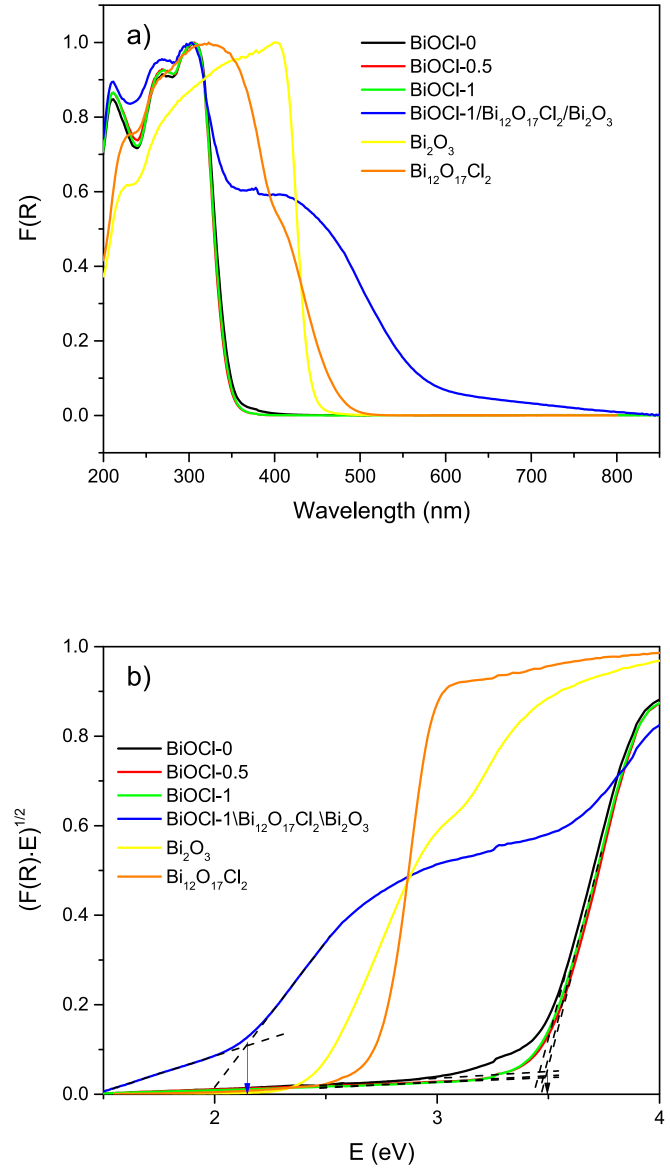

Fig. 2. (a) DRUV–Vis spectra and (b) plots of transformed Kubelka-Munck function vs. photon energy (eV) of bismuth-based materials.

The field emission scanning electron microscopy (FESEM) analysis confirms the formation of sheet-like structures for both samples BiOCl-1 and BiOCl-1/$Bi_{12}O_{17}Cl_2$/Bi_2O_3 (Fig. 3 and Fig. S5). Additionally, EDS mapping reveals the good distribution of Bi, O and Cl atoms in the composite (Fig. S6). High-resolution transmission electron microscopy (HRTEM) images allow identifying the coexistence of the three components (Fig. 4). Distances of 3.4 and 3.8 Å are discernible in the zone labeled as **A** in Fig. 4a, indicating the presence of the BiOCl phase [32]. Additionally, areas with periodicity of 8.8 Å (labeled **B**) reveal the presence of the $Bi_{12}O_{17}Cl_2$ phase [33]. Finally, a third type of crystal can be observed (labeled **C**), with distance values of 3.1 and 3.4 Å, corresponding to the Bi_2O_3 phase [34]. These features are further confirmed by the respective Fourier transforms performed on each area (Fig. 4b, c and d, respectively). Furthermore, the local EDS analysis reveals variations in the Bi:Cl ratio in each area (Fig. 4e). No chlorine is detected in area **C**, as expected for bismuth (III) oxide Bi_2O_3. A Bi:Cl ratio close to 50:50 and 86:14 is observed in areas **A** and **B**, respectively (Fig. 4f), which confirms the presence of the bismuth oxyhalides BiOCl and $Bi_{12}O_{17}Cl_2$. These results demonstrate the successful fabrication of the ternary composite between BiOCl, $Bi_{12}O_{17}Cl_2$ and Bi_2O_3 (Fig. S7).

The composition and chemical states of BiOCl-1 and BiOCl/$Bi_{12}O_{17}Cl_2$/Bi_2O_3 as representative samples were analysed by X-ray photoelectron spectroscopy (XPS). The full spectra of both materials are depicted in Fig. S8, revealing the elemental composition of the materials, including the signals corresponding to Bi, O, C, and Cl atoms. These signals appear quite similar in both spectra. The binding energy of the survey and the positions of the signals were calibrated and corrected through the C 1 s signal at 284.8 eV, derived from the test instrument itself. In the Bi 4f signal range (Fig. 5a), the BiOCl-1 sample shows a narrow doublet Bi $4f_{7/2}$ and Bi $4f_{5/2}$ around 159.6 and 165.0 eV, respectively, indicating the presence of Bi^{3+}. On the contrary, the ternary composite Bi 4f signal is significantly broad due to various contributions. Upon detailed analysis, both Bi $4f_{7/2}$ and Bi $4f_{5/2}$ peaks could be deconvoluted into three signals with a binding energy difference of about 1 eV which could be assigned to the three Bi^{3+} species present in the ternary composite. At lower binding energy, the doublet at 157.5 and 162.8 eV corresponds to Bi^{3+} in Bi_2O_3 [35], while the signals at 158.4 and 163.7 eV could be attributed to Bi^{3+} in $Bi_{12}O_{17}Cl_2$ [36]. The remaining Bi 4f peaks at 159.5 and 164.9 eV are ascribed to Bi^{3+} in BiOCl, consistent with the observed doublet in the BiOCl-1 spectrum and the predominant contribution of this material in the composite. Similarly, in the Cl 2p spectra of both samples (Fig. 5b), the doublet Cl $2p_{3/2}$ and Cl $2p_{1/2}$ is inferred under the envelope. Thus, the peaks around 198.4 and 200.0 eV are assigned to the chlorine in BiOCl for both samples, and the small signals at lower binding energy are also indexed to the characteristic peaks of Cl $2p_{3/2}$ and Cl $2p_{1/2}$, which could be ascribed to Cl in $Bi_{12}O_{17}Cl_2$, in the case of the composite [15]. These results demonstrate the simultaneous presence of the three different semiconductors in the ternary composite, as supported by HRTEM analysis, forming a stable and robust heterojunction, which is essential for an effective transfer of photogenerated charges.

Due to the rich electrochemical properties exhibited by bismuth-based materials, we performed solid-state electrochemical studies on the ternary composite BiOCl-1/$Bi_{12}O_{17}Cl_2$/Bi_2O_3, as well as, on the

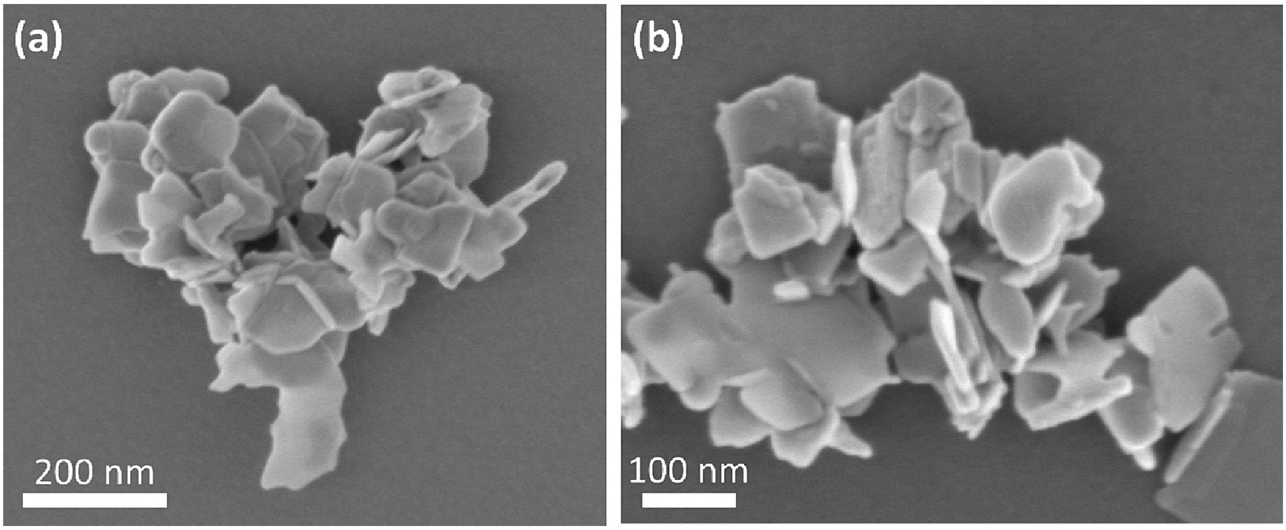

Fig. 3. FESEM images of the BiOCl-1/$Bi_{12}O_{17}Cl_2$/Bi_2O_3 composite.

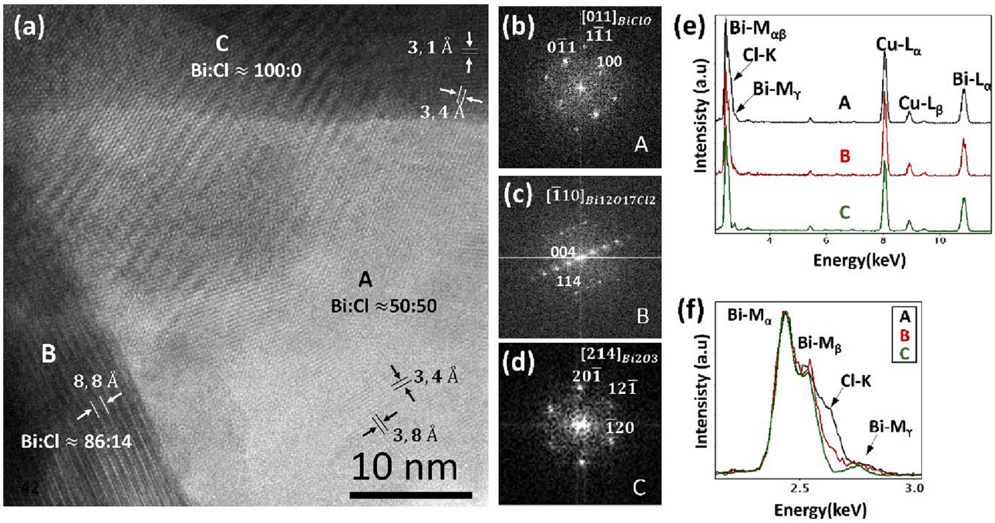

Fig. 4. A) hrtem image of the biocl-1/$bi_{12}O_{17}Cl_2$/Bi_2O_3 composite. Different phases are identified in areas A (BiOCl), B ($Bi_{12}O_{17}Cl_2$) and C (Bi_2O_3). (b-d) Corresponding Fourier transforms are performed on each area. (e) EDS spectra acquired in areas A, B and C. (f) The enlarged energy window evidence variation in the chlorine content.

individual materials. The electrochemical behavior of the β-Bi_2O_3 electrode was investigated through cyclic voltammetry (CV) with scan rates ranging from 50 to 150 mV/s (Fig. 6a). As the scan rate increased, the peak current also increased, indicating excellent rate performance of the Bi_2O_3 electrode, facilitating a rapid Faraday reaction ($Bi^{3+} \leftrightarrow Bi^0$) (Fig. S9a). All CV curves displayed distinct redox peaks, with the presence of anodic and cathodic peaks at varying scan rates, suggesting the involvement of the ionic electrolyte and electrode material in the redox reactions. Thus, the broad reduction peak at −0.85 V is associated with the primary cathodic process, signifying the reduction of dissolved BiO_2^- species to Bi^0 through successive reactions involving different bismuth oxidation states. Anodic potential scans reveal multiple anodic peaks, corresponding to the oxidation of residual bismuth. At higher scan rates, the cathodic peak broadens and shifts negatively, while the two anodic peaks associated exhibit smaller positive shifts. According to Vivier and coworkers [37], at a scan rate of 50 mV/s, the peak at −0.21 V is attributed to the oxidation of Bi^0 located at the surface/solution interface, while the peak at 0.14 V corresponding to the oxidation of Bi^0 to Bi^{3+}. In both cases, the underlying mechanism involves the oxidation of Bi(0) to Bi(I) and the disproportionation of Bi(I) to Bi(III) and Bi(0). In slightly alkaline media, Bi^{3+} reacts with OH^- to form $Bi(OH)_3$/BiOOH, which subsequently evolves into Bi_2O_3. Differential pulse voltammetry (DPV), a more sensitive technique, has also been employed to characterize β-Bi_2O_3 (Fig. 6b). The scan toward negative potentials reveals the presence of two distinct peaks in this region, confirming the well-known reduction mechanism of Bi_2O_3 through redissolution and subsequent reduction and disproportionation steps [38]. The peak at a higher potential (less negative) is attributed to the reduction of adsorbed BiO_2^- at the electrode surface. Meanwhile, the peak at a lower potential, representing the process with the most significant charge exchange, corresponds to the primary cathodic process, which involves the reduction of dissolved BiO_2^- species to BiO_2^{2-}. This is followed by the disproportionation of BiO_2^{2-} into BiO_2^- and Bi^0 in aqueous media.

The CV obtained with the BiOCl-modified CPE is shown in Fig. 7a. The obtained voltammogram reveals distinct cathodic peaks at −0.67 and −0.85 V when scanned at 50 mV/s, accompanied by less intense associated anodic peaks. These peaks correspond to the reduction of $[Bi_2O_2]^{2+}$ to Bi^0 through intermediate steps and subsequent reoxidation [23] (Fig. S9b). As the scan rate increases, the cathodic peak potential becomes more negative, and the peak current increases, as expected.

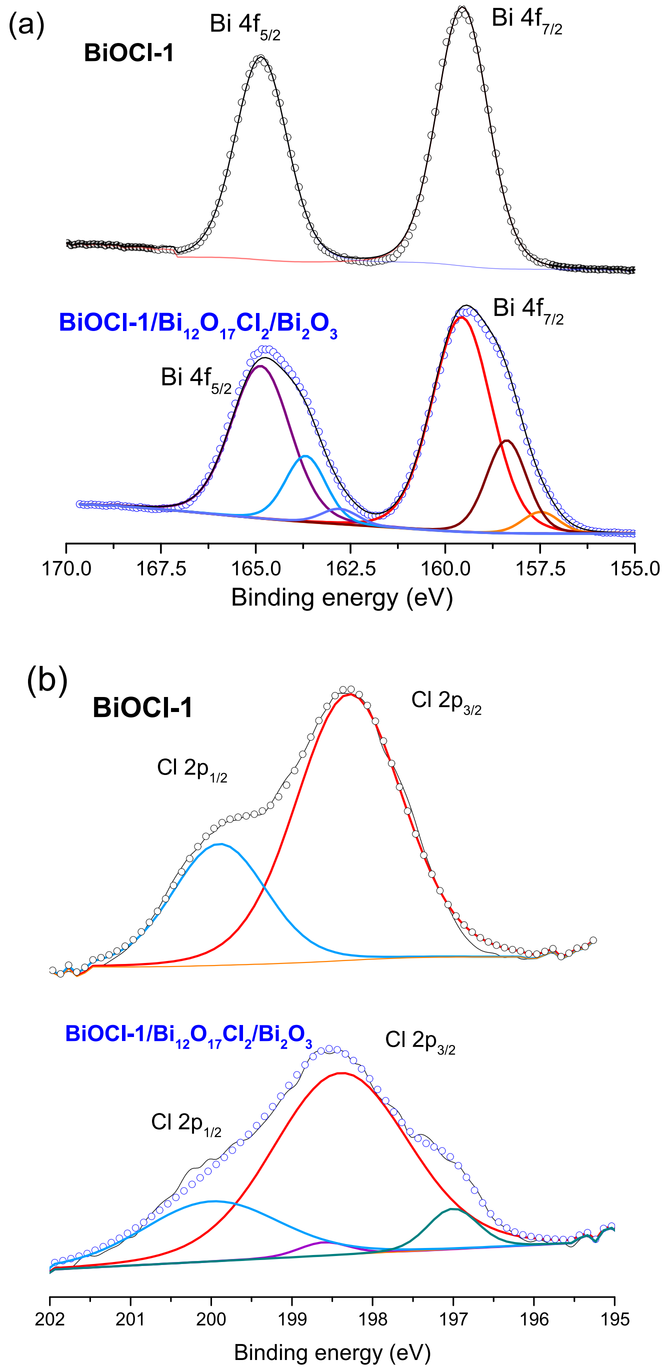

Fig. 5. XPS spectra of a) Bi 4f region and b) Cl 2p region for BiOCl-1 and BiOCl-1/$Bi_{12}O_{17}Cl_2/Bi_2O_3$ samples.

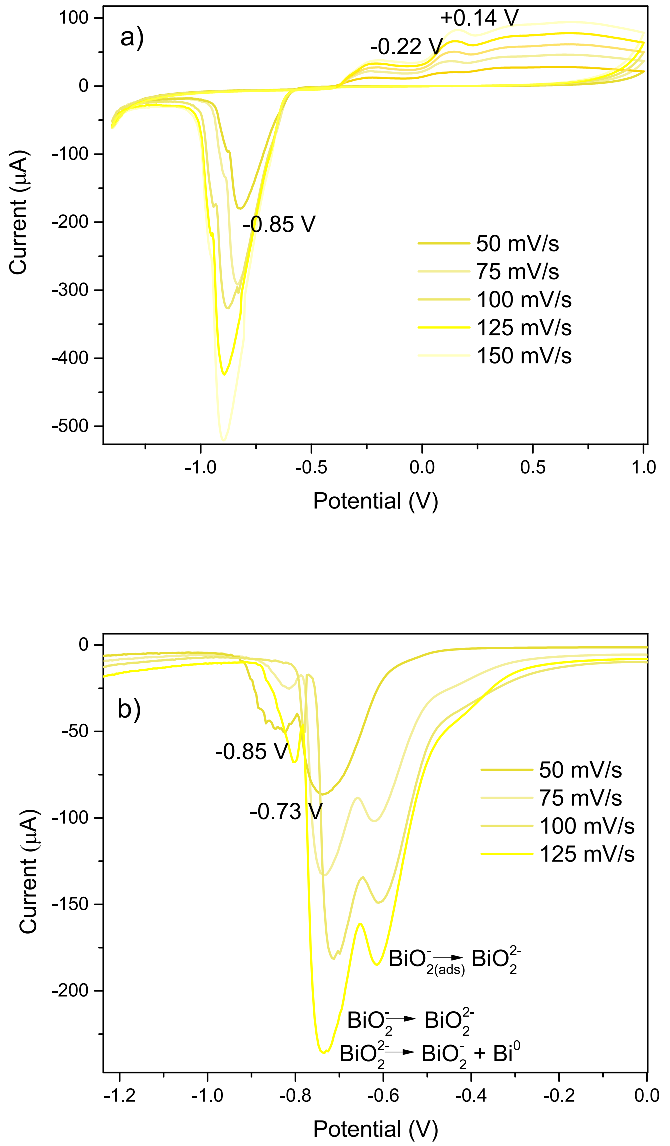

Fig. 6. A) cv and b) dpv of β-Bi_2O_3 carbon modified electrode as working electrode in 0.2 M Na_2SO_4 vs an Ag/AgCl/KCl (3 M) reference electrode and a platinum rod as counter electrode.

After several scans and measurements at higher scan rates, the peak associated with adsorbed bismuth species is no longer detected, only a broad peak is observed, attributed to the more abundant species in the solution, similar as previously reported [39]. In the anodic direction, a shift in the oxidation potential is observed, indicating that the oxidation potential is close to the metal/metal ion equilibrium potential. This is because the oxidation of metallic bismuth initiates from the surface with deposited metal. The presence of this crossover in the voltammograms serves as a reliable diagnostic tool for confirming the formation of bismuth metal on the electrode surface. Similar behavior was found in other reported works [40], where the higher deposition potential of metallic bismuth on a foreign substrate was explained by nucleation overvoltage due to crystallographic substrate-metal misfit. If the chemical step is slow enough to be outpaced by the scan, the ECE mechanism will result in a trace crossover. DPV measurements for BiOCl-1 at negative potentials (Fig. 7b) confirm the presence of two prominent peaks at −0.67 and −0.85 V, validating the reduction mechanism of BiO^+ species to Bi^0 with different locations, adsorbed and in solution through successive reaction steps.

Fig. 8a displays the CV measured for the non-stoichiometric $Bi_{12}O_{17}Cl_2$ material under similar experimental conditions. The obtained voltammogram closely resembles that obtained from BiOCl-1, featuring well-defined cathodic peaks at −0.70 and −0.85 V when scanned at 50 mV/s, accompanied by less intense associated anodic peaks, and exhibiting the presence of a crossover in the voltammogram. Differential pulse voltammetry (DPV) measurements confirm the presence of two main cathodic peaks at −0.70 and −0.85 V. However, in this case, the current peak intensity indicates the predominance of the first peak at −0.70 V. As previously discussed [37], the presence of multiple cathodic and anodic peaks in the cyclic voltammogram of β-Bi_2O_3 is due to the reduction/oxidation of BiO_2^-/Bi^0 species through similar redox mechanism but in different locations, they are adsorbed species on the surface/solution interface or the most abundant dissolved species,

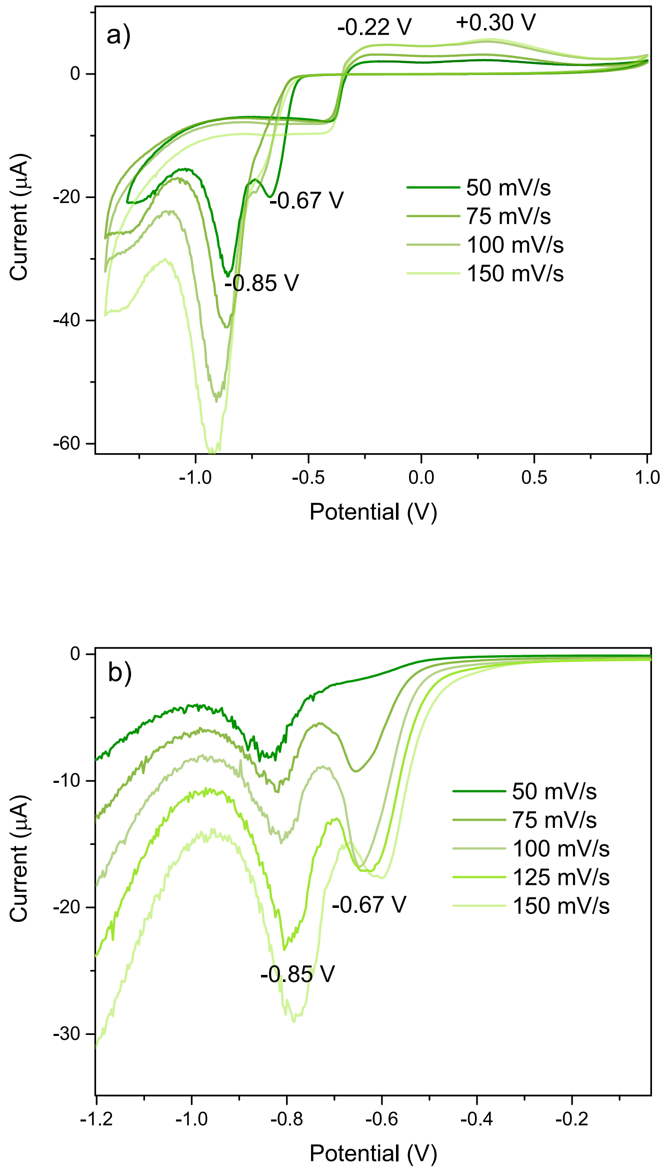

Fig. 7. A) cv and b) dpv of biocl-1 carbon modified electrode as working electrode in 0.2 M Na_2SO_4 vs an Ag/AgCl/KCl (3 M) reference electrode and a platinum rod as counter electrode.

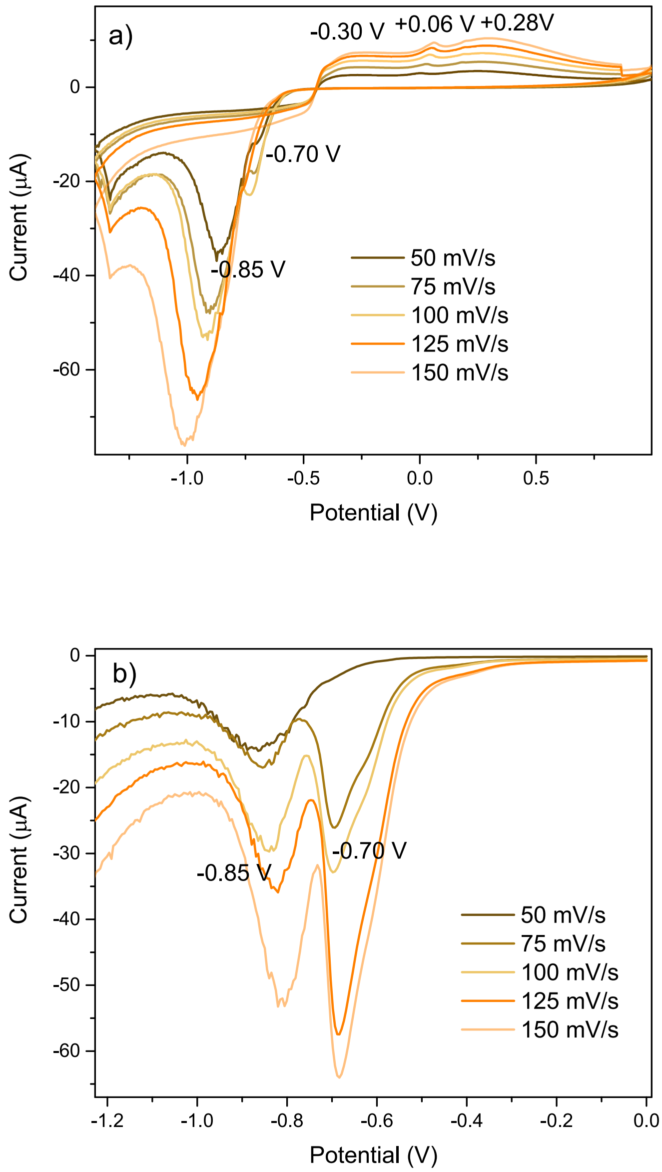

Fig. 8. A) cv and b) dpv of $bi_{12}O_{17}Cl_2$ carbon modified electrode as working electrode in 0.2 M Na_2SO_4 vs an Ag/AgCl/KCl (3 M) reference electrode and a platinum rod as counter electrode.

thereby their availability influences their chemical and electrochemical reactions. In the structure of BiOCl, the Bi atoms in the $[Bi_2O_2]^{2+}$ layers are exposed on the exterior, making them easily accessible. $Bi_{12}O_{17}Cl_2$, consisting of six $Bi_6O_{8.5}$ layers separated by a Cl layer, contains three distinct types of bismuth atoms (Fig. S9c). The O1 and O2 atoms in the outer sublayers occupy tetrahedral holes, forming a $[Bi_2O_2]$-type slab, while the inner O3-O6 atoms between the Bi sublayers, forming a $BiO_{2.25}$ slab, deviate from the expected positions, and no oxygen is found between the Bi sublayers. Most oxide anions are located at the octahedral sites, but some occupy tetrahedral holes, creating a $[Bi_2O_2]^{2+}$-like environment [28]. According to this structure, it can be inferred that Bi (III) in $[Bi_2O_2]^{2+}$ layers highly exposed are more likely to escape from the lattice compared to the inner atoms. In addition, Bi(III) species with similar a $[Bi_2O_2]^{2+}$-like environment in BiOCl and $Bi_{12}O_{17}Cl_2$ would yield cathodic and anodic peaks with similar reduction and oxidation potential values. However, the current peak intensities would differ due to the different proportions of Bi(III) atoms with $[Bi_2O_2]^{2+}$-like environment as observed in DPV for $Bi_{12}O_{17}Cl_2$ in Fig. 8b.

Finally, the ternary composite BiOCl-1/$Bi_{12}O_{17}Cl_2$/Bi_2O_3 was also investigated. The obtained voltammogram displayed well-defined cathodic peaks at −0.75 and −0.85 V when scanned at 50 mV/s, accompanied by less intense associated anodic peaks (Fig. 9a). As expected, with an increase in the scan rate, the cathodic peak potentials became slightly more negative, and the peak current increased. Similar to the behavior observed in BiOCl-1 and $Bi_{12}O_{17}Cl_2$ materials, a crossover in the oxidation potential was observed in the anodic direction, indicating the formation of bismuth metal on the electrode surface. The mechanism of reduction/oxidation appeared to be similar to that of the individual components, involving the reduction of Bi(III) species to metallic bismuth through the redissolution of solid-based bismuth materials, electrochemical reduction of dissolved species at different locations and disproportionation. DPV measurements reveal the existence of three peaks at −0.59, −0.67 and −0.85 V (Fig. 9b). The peak with the most negative potential value, −0.85 V, consistently appears in all voltammograms, irrespective of the nature of the material under investigation. As previously proposed, it can be attributed to the reduction of dissolved BiO_2^- (Bi(III) species). Meanwhile, the peaks at higher potentials (*i.e.* −0.59 and −0.67 V) can be ascribed to the

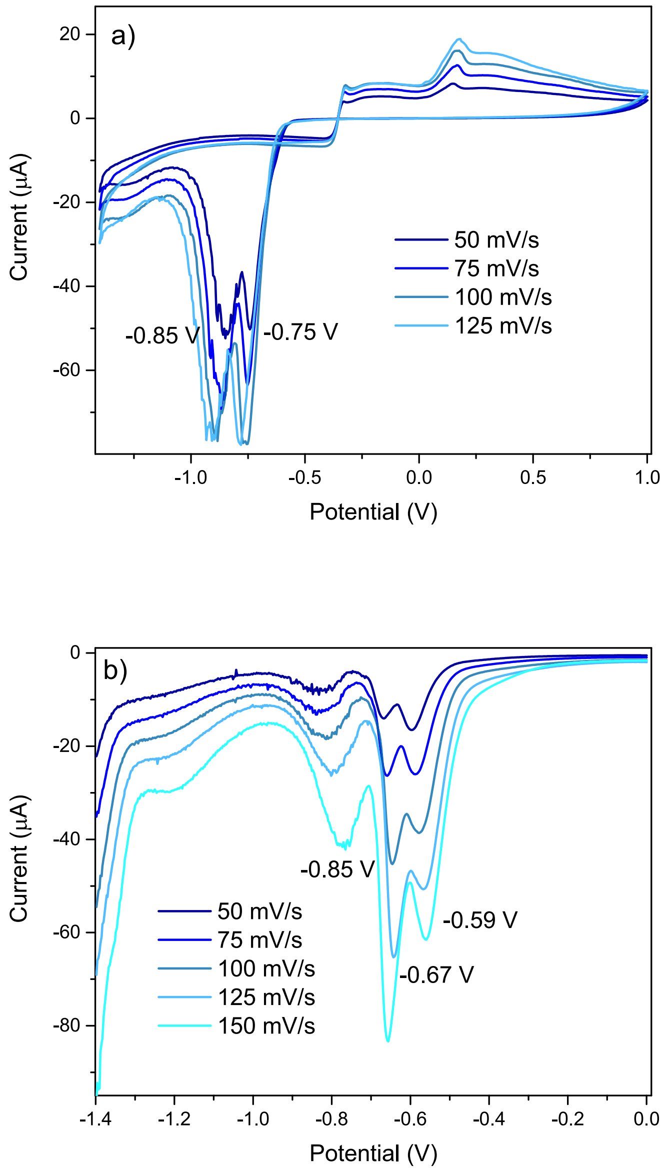

Fig. 9. A) cv and b) dpv of BiOCl-1/$Bi_{12}O_{17}Cl_2$/Bi_2O_3 carbon modified electrode as working electrode in nitrogen saturated aqueous 0.2 M Na_2SO_4 vs an Ag/AgCl/KCl (3 M) reference electrode and a platinum rod as counter electrode.

reduction of adsorbed bismuth species from various locations. The peak at −0.67 V may be associated with the chemical/electrochemical reaction of a $[Bi_2O_2]^{2+}$-like environment, species also found in BiOCl and $Bi_{12}O_{17}Cl_2$ materials. However, the ternary composite exhibits an additional signal at −0.59 V, which is absent in the individual components. Assuming, as in the individual materials, the presence of Bi(III) species with different locations and availability to generate adsorbed species facing the electrochemical reaction, the appearance of this signal indicates the presence of different structural Bi(III) species, specifically due to the formation of the heterojunction. Furthermore, the generated adsorbed species in the heterostructure reduce at the highest potential (the less negative), indicating higher Lewis's acid properties. This implies that bismuth metal centers with higher electron deficiency and, subsequently, more easily reduced. The electrochemical characteristics can tentatively be attributed to synergistic effects between the three components BiOCl-1, Bi_2O_3, and $Bi_{12}O_{17}Cl_2$, influencing both the electric conductivity of the materials and the chemical properties of the active centers. The presence of Bi(III) species in the framework with higher Lewis acidity may significantly enhance its adsorptive properties towards the reactants.

In addition, CV can also be utilized to assess the electrochemical ion exchange performance of these electrodes in the electrolyte solution. When a reduction potential is applied to the electrode, the bismuth material on the electrode acquires a negative charge. Simultaneously, sodium cations from the electrolyte are absorbed into the material to neutralize the negative charge. As previously mentioned, the single materials and the composite exhibit significant reduction peaks of Bi(III) species, which coincide with the incorporation of Na^+ ions. However, from the analysis of CV curves in Fig. 10a, it is evident that the BiOCl-1/$Bi_{12}O_{17}Cl_2$/Bi_2O_3 electrode shows a significantly larger redox peak area than BiOCl-1, indicating superior electrochemical activity and improved ion exchange performance for Na^+ of the composite.

Electrochemical impedance spectroscopy (EIS) measurements were conducted to assess the charge transfer kinetics at the interface between the carbon paste bismuth-based electrodes and the electrolyte solution (Fig. 10b). The frequency range covered from 100 kHz to 0.1 Hz, and the

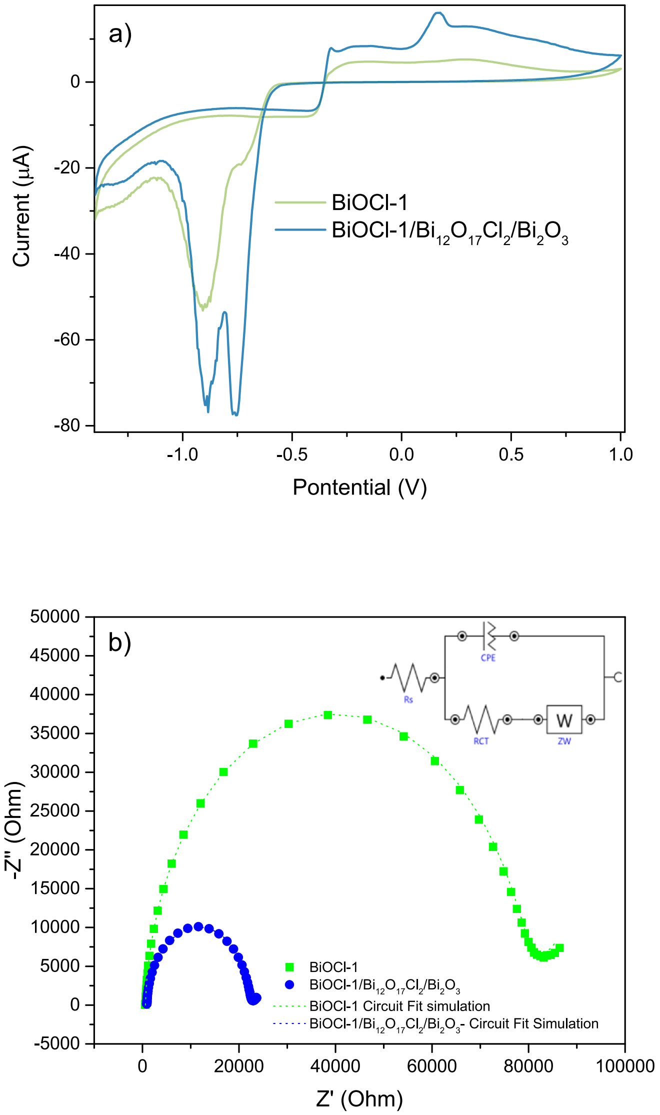

Fig. 10. A) cv of biocl-1 and BiOCl-1/$Bi_{12}O_{17}Cl_2$/Bi_2O_3 carbon paste electrodes from 1 to −1.4 V at a scan rate of 100 mV/s in 0.2 M Na_2SO_4 solution. b) Electrochemical impedance measurements, Nyquist plots ($E_{applied}$ = OCP vs Ag/AgCl) of the BiOCl-1/$Bi_{12}O_{17}Cl_2$/Bi_2O_3 and BiOCl-1 carbon paste electrodes in 5×10^{-3} mol L^{-1} $K_3Fe(CN)_6$ + 0.1 mol L^{-1} KOH with an AC amplitude of 10 mV and frequency range of 0.1 to 100 000 Hz.

measurements were performed in the presence of the molecular redox probe $[Fe(CN)_6]^{3-/4-}$. The performance of BiOCl-1/$Bi_{12}O_{17}Cl_2$/Bi_2O_3 was compared to that of pristine BiOCl-1, which served as the starting material. For the EIS analysis, an equivalent Randles model circuit was employed, modulated with R_S, R_{ct}, CPE, and Z_W elements (as shown in the inset of Fig. 10b). Here, Rs represents the resistance associated with the conductive substrate, external electrical connections, and the electrolyte solution. R_{ct} corresponds to the direct charge-transfer resistance at the electrode/electrolyte solution interface. CPE, or constant phase element, is used to model non-ideal capacitance behavior arising from factors such as surface roughness, non-uniformity, or surface porosity of the electrode. Finally, Z_W the Warburg resistance is a result of diffusion processes taking place at the electrode–electrolyte interface [37,41]. As can be seen in the Nyquist plots (Fig. 10b), both materials exhibit well-defined semicircles and a minor linear slope, indicating that the process is primarily controlled by charge-transfer resistance. BiOCl-1/$Bi_{12}O_{17}Cl_2$/Bi_2O_3 clearly demonstrates lower resistance and more efficient charge transfer, consistent with the findings from CV measurements. The R_{ct} values, representing the resistance of the electrode/electrolyte solution interface, were estimated from the semicircular portion of the Nyquist plot. The Nyquist diagram displays a smaller semicircle radius for the ternary composite. Specifically, R_{ct} values for BiOCl-1/$Bi_{12}O_{17}Cl_2$/Bi_2O_3 and BiOCl-1 are 21.5 and 77.9 kΩ, respectively. The reduced resistance observed in the ternary composite suggests an enhanced electronic and ionic conduction, factors that can significantly promote the photocatalytic activity of the material.

Similarly, photocurrent experiments of the ternary composite were measured. The results are shown in Fig. 11, alongside those of BiOCl-1, $Bi_{12}O_{17}Cl_2$ and Bi_2O_3 for comparison. As can be seen in the Fig. 11, all materials exhibit a good response to visible light. However, BiOCl-1/$Bi_{12}O_{17}Cl_2$/Bi_2O_3 displays the most significant light response, exhibiting a current density that is up to 0.4 μA/cm^2 higher than its individual components.

3.2. Photocatalytic degradation of single contaminants under visible light

To assess the visible-active photoactivity performance of the bismuth-based materials, relevant contaminants were chosen. For instance, the antibiotic CIP is detected at high concentrations in water (around 50 % of the oral dose is excreted in the urine [42]), provoking antibiotic resistance [43]; the personal care MP is frequently used in cosmetics, pharmaceuticals and food as a preservative, being found in certain aquatic compartments [44] and correlated with the risk of breast cancer [45]; and the azo dye MO, as a model dye pollutant, can cause carcinogenic effects on aquatic organisms and humans [46].

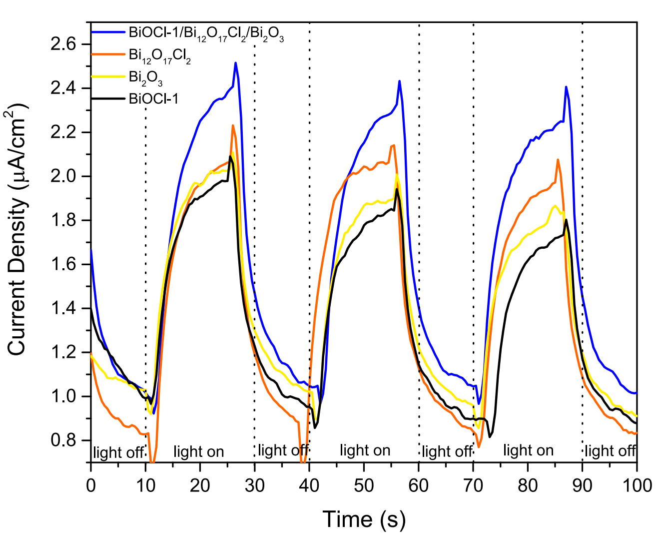

Fig. 11. Photocurrent density of BiOCl-1/Bi_2O_3/$Bi_{12}O_{17}Cl_2$, BiOCl-1, Bi_2O_3, and $Bi_{12}O_{17}Cl_2$ at a potential of 1.0 V (V vs Ag/AgCl) under visible light ($\lambda >$ 400 nm).

3.2.1. Photocatalytic degradation of CIP

Firstly, the photocatalytic experiments were accomplished on bismuth-based samples using 20 mL of a CIP solution (15 ppm) under visible light. As can be seen in Table 2, the adsorption capacity of BiOCl-1 was remarkably higher than that achieved for BiOCl-0 (71 % vs 26 %), suggesting that the use of ionic liquid may influence the adsorption capacity of BiOCl samples. To shed more light on the adsorption process, the zeta potential of BiOCl samples was determined at solution pH (pH = 7.4) (Table 2), resulting in −26.6, −27.1, and −27.3 for BiOCl-0, BiOCl-0.5 and BiOCl-1, respectively. This indicates that the use of ionic liquid has only a slight effect on the surface charge of the materials. A similar zeta potential was found for the composite (-27.6), which was able to adsorb 34 % of CIP. Therefore, the effect of the specific surface area seems to be the main factor in the adsorption process, enhancing the adsorption ability of BiOCl-1 ($S_{BET} = 37.84$ m^2/g and $V_p = 0.17$ cm^3 g^{-1}) and the BiOCl-0.5 ($S_{BET} = 31.25$ m^2/g and $V_p = 0.17$ cm^3 g^{-1}). It is important to note that the BiOCl-1/$Bi_{12}O_{17}Cl_2$/Bi_2O_3 composite exhibited a superior visible-light photocatalytic activity, reaching a CIP removal of 95.2 % in only 40 min (Fig. 12). The photodegradation of CIP follows a pseudo-fist-order kinetic for all the bismuth-based samples (Fig. S10a) and the kinetic constants are shown in Table 2. The best value was found for the ternary composite photocatalyst ($k = 0.0703$ min^{-1}), which is 4.7 and 1.4 times higher that obtained for the single samples BiOCl-0 ($k = 0.0149$ min^{-1}) and BiOCl-1 ($k = 0.0508$ min^{-1}), respectively. Thus, the superior photocatalytic performance of the ternary composite is attributed to its excellent optical properties (*i.e.* low recombination of electron-hole pairs) and enhanced electronic and ionic conduction (*i.e.* reduced resistance and enhanced charge transfer efficiency), as observed in the characterization studies. Comparing our composite with other reported systems, BiOCl-1/$Bi_{12}O_{17}Cl_2$/Bi_2O_3 demonstrates a faster degradation of CIP compared to that reported for CdS/BiOBr ($k = 0.01729$ min^{-1}) [47] or $FeWO_4$/nitrogen-doped carbon ($k = 0.024$ min^{-1}) [48] or even the dual Z-scheme composite 75 % $NiFe_2O_4$/Bi_2WO_6/AgI ($k = 0.0625$ min^{-1}) [49] among others (see Table S1).

3.2.2. Photocatalytic degradation of MO and MP

To further study on visible-light photocatalytic performance of BiOCl-1/$Bi_{12}O_{17}Cl_2$/Bi_2O_3, the removal of MO and MP were also evaluated. For the elimination of MO, the composite exhibited an exceptional adsorption capacity (Fig. 13), removing up to 80 % of the dye in only 30 min under darkness. When the visible light was applied, the ternary composite photocatalyst showed a complete MO removal in 10 min ($k = 0.075$ min^{-1}) (Fig. S10b). On the contrary, a reduced adsorption capacity was observed for BiOCl-1/$Bi_{12}O_{17}Cl_2$/Bi_2O_3 in the case of MP, as it demonstrated the ability to eliminate MP by a photocatalytic process (99.6 % removal in 30 min, $k = 0.176$ min^{-1}) (Fig. S10c). Compared to other bismuth-based photocatalysts reported in the literature, BiOCl-1/$Bi_{12}O_{17}Cl_2$/Bi_2O_3 exhibited a higher removal efficiency for MP and MO (Table S1).

3.2.3. Effect of initial pH, organic matter and inorganic species on the degradation process

The impact of initial pH value and the presence of organic and inorganic species on the photocatalytic degradation of CIP and MP were investigated. As can be seen in Fig. 14a, the pH value has different effects on the degradation of CIP and MP. Hence, the removal of CIP decreased from 95.2 % to 83.7 % at a pH = 4, while it remained stable at a pH = 8 (95.2 % vs. 94.6 %). This could be explained based on the pK_a values of CIP (pK_a = 6.09 and 8.62) [50], indicating that this contaminant exists as a zwitterion at pH = 6.4 and pH = 8, promoting the adsorption and contact with the material, which is negatively charged (see Table 2). In

Table 2
Removal of CIP using the as-prepared bismuth-based photocatalysts.

Catalyst	Adsorption capacity (%)	Zeta potential	Removal efficiency (%)	k (min^{-1})	Time (min)
BiOCl-0	26	−26.6	80.6	0.0149	60
BiOCl-0.5	62	−27.1	92.6	0.0279	60
BiOCl-1	71	−27.3	95.7	0.0508	60
BiOCl-1/$Bi_{12}O_{17}Cl_2$/Bi_2O_3	34	−27.6	95.2	0.0703	40

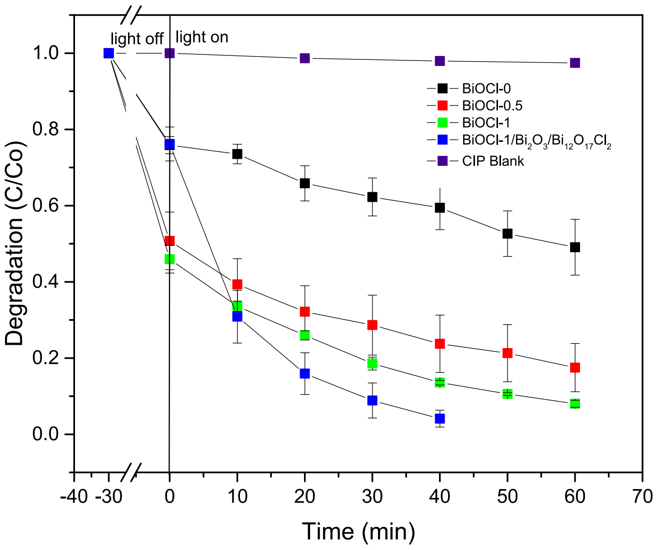

Fig. 12. Degradation of CIP using bismuth-based photocatalysts under visible light.

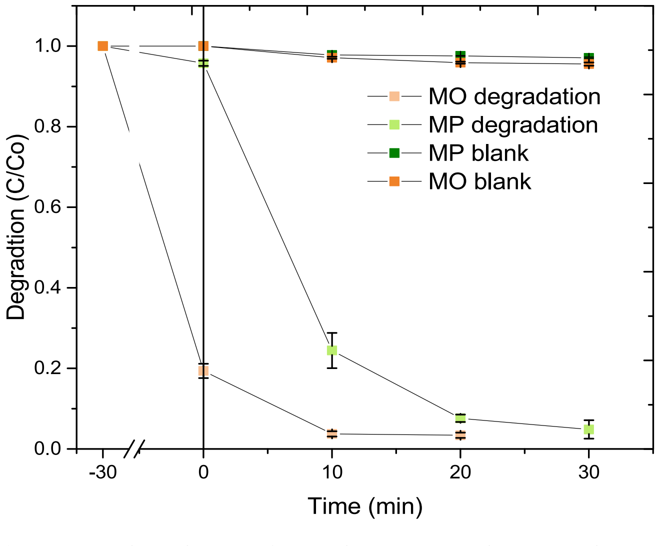

Fig. 13. Degradation kinetics of MO and MP using BiOCl-1/$Bi_{12}O_{17}Cl_2$/Bi_2O_3 photocatalyst under visible light.

contrast, the degradation of MP significantly decreased at a pH = 8 (from 99.6 % to 51.7 %), but it remained constant at a pH = 4 (99.6 % vs. 99.5 %). MP has a pK_a value of 8.5 [51], and is probably present in its neutral form at pH = 8. This suggests that the degradation process involves not only electrostatic interactions between photocatalyst and contaminant but also other types of interactions (*i.e.* hydrogen bonds).

The effect of organic and inorganic species on the degradation process was evaluated using humic acid (HA) (1 mg/L) as an organic matrix and HCO_3^- as an inorganic species (0.5 mM) [52]. In presence of HA, the photodegradation of both CIP and MP only slightly decreased (95.2 % vs. 93.8 % for CIP and 99.6 % vs. 92.8 % for MP) (Fig. 14b). However, a notable impact was observed in the presence of HCO_3^-, with the efficiency decreasing to 85.2 % and 86.9 %, for CIP and MP, respectively. These results may be attributed to a possible competition between HCO_3^- and the contaminants. Note that the photodegradation still reached more than 85 % at 30 and 40 min for CIP and MP, respectively.

3.2.4. *Stability and reusability studies*

To evaluate the stability and reusability of the photocatalyst, four successive cycles of 20 min each were performed (Fig. S11) in which MO was almost completely removed (>80 % removed after 4 cycles). In addition, PXRD analysis confirmed that the structure of BiOCl-1/$Bi_{12}O_{17}Cl_2$/Bi_2O_3 photocatalyst was preserved after 4 cycles under visible light irradiation (see Fig. S12), proving the excellent chemical stability of BiOCl-1/$Bi_{12}O_{17}Cl_2$/Bi_2O_3 photocatalyst to be used as a visible-light active photocatalyst. To complete the stability study, recycling tests were also carried out for up to 3 cycles for both MP and CIP individual degradation (Fig. S13). In the case of CIP, the ternary composite exhibited a degradation of more than 85 % for all of them. Whereas, for MP degradation, there was a notable decrease in photoactivity by the third cycle, with degradation dropping to 50 %.

3.2.5. *Degradation mechanism and scavenger studies*

To further understanding of the degradation process by BiOCl-1/$Bi_{12}O_{17}Cl_2$/Bi_2O_3 photocatalyst, scavengers such as isopropyl alcohol (IPA), ascorbic acid (AA) or benzoquinone (BQ) were added to quench hydroxyl radicals ($^{\bullet}OH$), positive holes (h^+), and superoxide radicals ($O_2^{\bullet -}$), respectively (Fig. S14). Clearly, the photocatalytic process for MP was not affected by the addition of IPA, while the presence of AA and BQ suppresses the degradation. This indicates that $O_2^{\bullet -}$ is the primary reactive specie involved in the process and h^+ also contributes. The generation of hydroxyl radicals is not possible since the standard redox potential of Bi^{5+}/Bi^{3+} (1.59 V) that is less positive than that of $^{\bullet}OH/OH^-$ (1.99 V). Both reactive species (h^+ and $O_2^{\bullet -}$) were also identified by Xiao et al. [53] for the degradation of various parabens on I-doped $Bi_4O_5Br_2$.

To get more detailed information about the degradation process of both CIP and MP by BiOCl-1/$Bi_{12}O_{17}Cl_2$/Bi_2O_3, the degradation intermediates were identified using LC-MS, and possible degradation pathways were proposed. Since the MP degradation process is fast, only a few intermediates were detected (Fig. S15 and Fig. S16). In this regard, the most common degradation pathways start with the addition of a hydroxyl group via an attack of hydroxyl radicals [54]. Similarly, in this work, the detection of the compound MP-1 (m/z = 169) confirms a similar pathway, but the presence of the hydroxyl group is caused by the direct oxidation of the holes, followed by the attack of the superoxide radicals [55]. Thus, the intermediate MP-2 (m/z = 138) can be due to the loss of the methyl group from the ester moiety. Then, MP-2 is converted to malonic acid (MP-3 m/z = 104) via oxidation, followed by the mineralization to CO_2 and H_2O.

3.2.6. *Toxicity of degradation intermediates*

In the possible degradation pathway of CIP (Fig. S17 and S18), firstly, the formation of the compound CIP-1 (m/z = 305) can be explained by the oxidation of piperazine followed by ring opening. Then, the formation of the intermediate product CIP-4 (m/z = 244) can

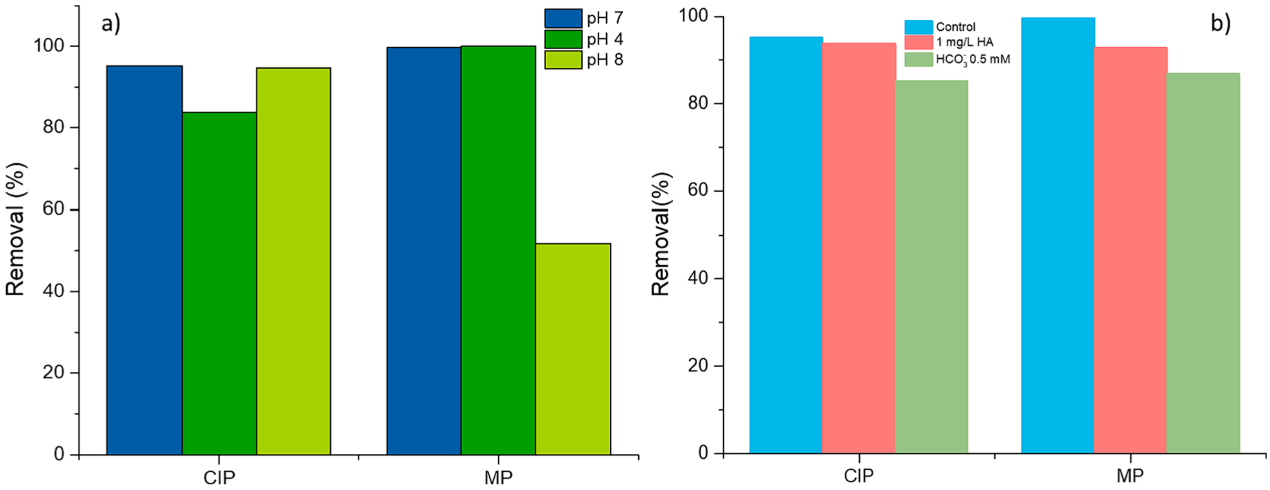

Fig. 14. Effect of a) initial pH and b) matrix water on the degradation process of CIP and MP under visible light using BiOCl-1/$Bi_{12}O_{17}Cl_2$/Bi_2O_3 photocatalyst for 40 and 30 min for CIP and MP, respectively.

occur in two ways: the loss of the group C_2H_5N of CIP-2 (m/z = 262) and the latter defluorination of the other way around though CIP-3 (m/z = 287), as both CIP-2 and CIP-3 are observed [56]. Subsequently, the compound CIP-4 suffers a decarboxylation process to generate the product CIP-5 (m/z = 216) followed by the loss of both alcohol and amino groups [57]. Finally, the peak associated to the compound CIP-7 is detected before the mineralization into CO_2 and H_2O.

To assess the removal efficiency, it is crucial to examine the toxicity

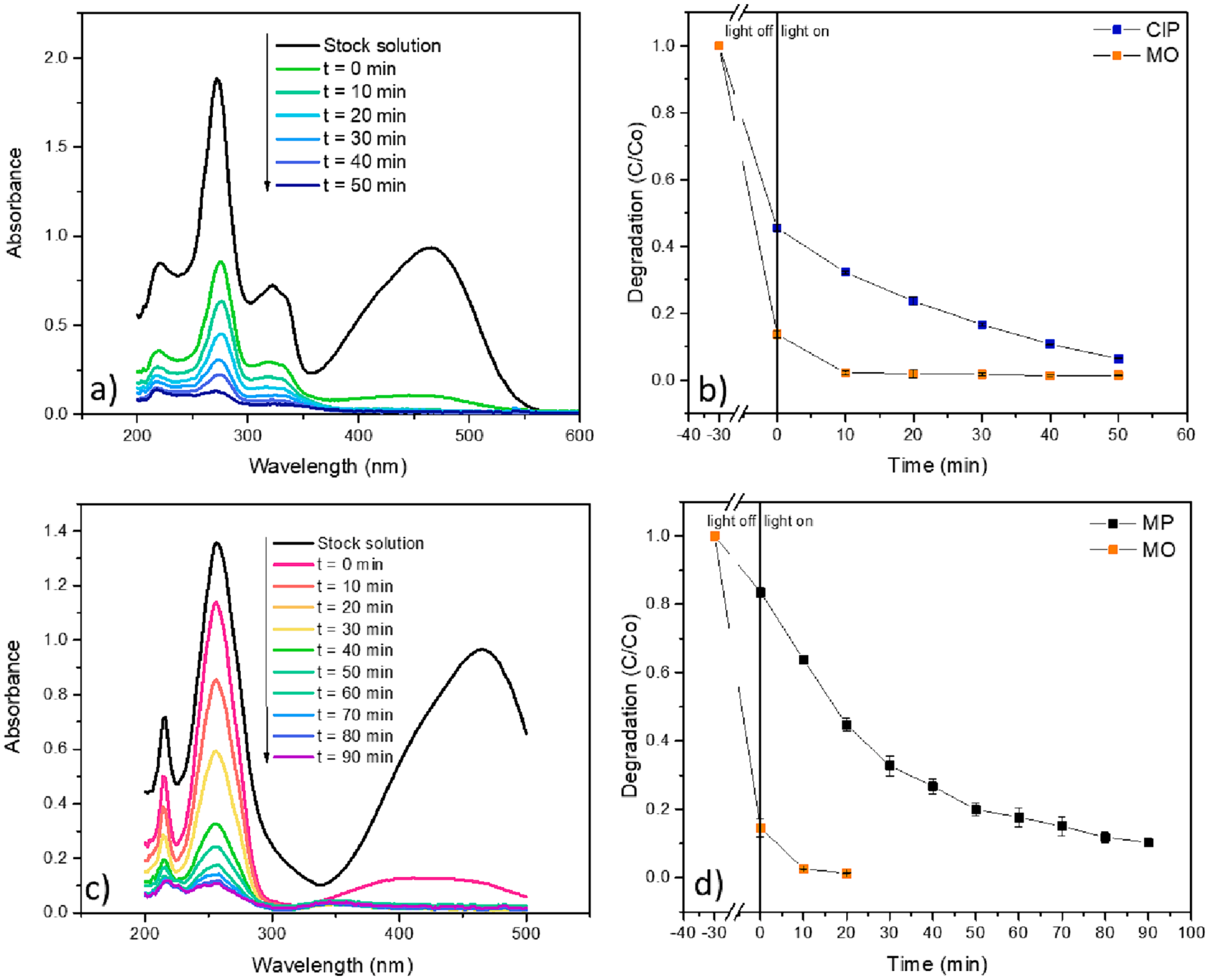

Fig. 15. Time-dependent UV–vis during photodegradation process and degradation kinetics of a) and b) a mixture of CIP and MO and c) and d) a mixture of MP and MO using the BiOCl-1/$Bi_{12}O_{17}Cl_2$/Bi_2O_3 photocatalyst under visible light.

of the degradation intermediates. For example, some drugs such as ibuprofen and salicylic acid can generate highly toxic intermediates [58]. The Toxicity Estimation Software Tool (T.E.S.T.), developed by the Environmental Protection Agency of the USA, was used to evaluate the toxicity of the degradation products. The toxicity was predicted based on the fathead minnow (fish) EC_{50} (96 h). The resulting toxicity of the contaminants and their intermediates are shown in Table S2. As expected, the CIP drug is considerably more toxic than the MP molecule, as well as their corresponding degradation products. Both degradation processes evolve products that are less toxic or entirely non-toxic, attaining the main challenge of a photodegradation process.

3.3. Photocatalytic degradation of binary mixtures of contaminants under visible light

The simultaneous photocatalytic degradation of mixtures of CIP/MO or MP/MO was also carried out using the BiOCl-1/$Bi_{12}O_{17}Cl_2$/Bi_2O_3 photocatalyst (Fig. 15), revealing an excellent adsorption capacity of the composite for CIP and MO, consistent with observations in single photodegradation experiments. Importantly, the removal of CIP and MO was not affected by the presence of another contaminant, as evidenced by similar removal profiles compared to the single-contaminant experiments. Thus, BiOCl-1/$Bi_{12}O_{17}Cl_2$/Bi_2O_3 degraded both contaminants within 50 min (Fig. 15a and b). Conversely, the photodegradation of MP declined compared to single MP degradation (from 95.5 % to 68 % in 30 min), reaching almost complete degradation in 90 min (Fig. 15c and d). This could be explained by the presence of MO on the photocatalyst surface which might slow down the degradation of MP.

3.4. Photocatalytic mechanism

Finally, the energy levels of conduction band potential (E_{CB}) and valence band potential (E_{VB}) for the bismuth-based materials were calculated from CV measurements (Fig. S19) according to the following equations:

$$E_{LUMO(CB)} = -(E_{red} + 4.4)eV \quad (1)$$

$$E_{HOMO(VB)} = E_{LUMO} - E_g \quad (2)$$

$$E_g = 1240/\lambda_g \quad (3)$$

where E_{red}, in Eq. (1) is the onset reduction potential relative to Ag/AgCl/KCl (3 M), obtained from the CV of the material. The value 4.4, is the energy level of the Ag/AgCl/KCl (3 M) used as a reference electrode relative to the vacuum level. Correspondingly, the valence band potential (E_{VB}) was calculated according to the formula (2), where E_g is the optical band gap of the material calculated from the DRUV–Vis spectra, through the absorption edge of the material (λ_g) and using Eq. (3). The proposed mechanism for the photocatalytic process is shown in Fig. 16. When visible light is applied, $Bi_{12}O_{17}Cl_2$ and Bi_2O_3 phases are successfully excited (*i.e.* band gap values 2.61 and 2.58 eV, respectively) resulting in the generation of electron-hole pairs. Therefore, the photogenerated electrons react with O_2 forming superoxide radicals, as the CB values are more negative than the redox potential O_2/ $O_2^{\bullet-}$. Besides, the CB values of $Bi_{12}O_{17}Cl_2$ and Bi_2O_3 are more negative than the CB of BiOCl-1, thus photogenerated electrons may migrate to the BiOCl-1 phase, inhibiting the recombination of photogenerated electron-hole pairs in the ternary composite (Fig. 16). This is accordance with what was revealed from trapping experiments, superoxide radicals are the primary reactive species, along with holes during the photocatalytic process.

4. Conclusions

A sustainable and visible-light-driven photocatalyst has been fabricated by two-step precipitation-hydrothermal method, ensuring the formation of an intimate heterojunction with high carrier separation efficiency and enhanced electronic and ionic conduction. Therefore, BiOCl-1/$Bi_{12}O_{17}Cl_2$/Bi_2O_3 photocatalyst exhibited impressive photodegradation performance for both single pollutants and binary mixtures. According to the resulting degradation products, the ternary composite degraded CIP and MP into safer compounds. The quenching experiments revealed that superoxide radicals are the primary reactive species, along with the participation of holes. As evidenced by CV experiments, the ternary composite showed superior electrochemical activity and improved ion exchange performance for Na^+ compared to that observed for BiOCl-1.

CRediT authorship contribution statement

Helena Pérez del Pulgar: Writing – original draft, Methodology, Investigation, Conceptualization. **Josefa Ortiz-Bustos:** Methodology, Investigation. **Almudena Torres-Pardo:** Methodology, Investigation. **Marina Parras:** Methodology, Conceptualization. **Isabel del Hierro:** Supervision, Methodology, Conceptualization. **Yolanda Pérez:** Writing – original draft, Supervision, Funding acquisition, Conceptualization.

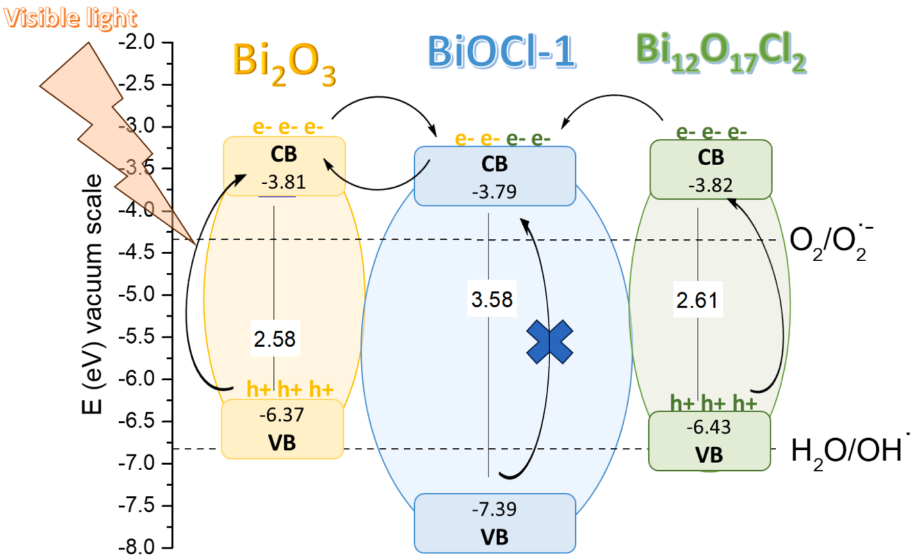

Fig. 16. Proposed photocatalytic mechanism.

Declaration of competing interest

The authors declare that they have no known competing financial interests or personal relationships that could have appeared to influence the work reported in this paper.

Data availability

Data will be made available on request.

Acknowledgements

Y.P., I.H., H.P.dP. and J.O.-B. gratefully acknowledge financial support from MCIN/AEI/10.13039/501100011033 and “ERDF A way of making Europe” (project PID2022-136417NB-I00) and M.P. and A.T.-P. from Comunidad de Madrid through the PR65/19-22438 project.

Appendix A. Supplementary material

Supplementary material to this article can be found online at https://doi.org/10.1016/j.apsusc.2024.160028.

References

[1] Z. Ali, J. Ma, M. Hong, R. Sun, Review: applications of the functional photocatalysts BiOX (X = Cl, Br, I) for clean energy, the environment, and future photobiorefineries, J. Mater. Chem. A. 11 (2023) 3297–3314, https://doi.org/10.1039/D2TA09877F.

[2] M. Shahbazi, L. Faghfouri, M.P.A. Ferreira, P. Figueiredo, H. Maleki, F. Sefat, J. Hirvonen, H.A. Santos, The versatile biomedical applications of bismuth-based nanoparticles and composites: therapeutic, diagnostic, biosensing, and regenerative properties, Chem. Soc. Rev. 49 (2020) 1253–1321, https://doi.org/10.1039/C9CS00283A.

[3] W. Zhang, X. Dong, Y. Liang, Y. Sun, F. Dong, Ag/AgCl nanoparticles assembled on BiOCl/$Bi_{12}O_{17}Cl_2$ nanosheets: enhanced plasmonic visible light photocatalysis and in situ DRIFTS investigation, Appl. Surf. Sci. 455 (2018) 236–243, https://doi.org/10.1016/j.apsusc.2018.05.171.

[4] Y. Liu, B. Yang, H. He, S. Yang, X. Duan, S. Wang, Bismuth-based complex oxides for photocatalytic applications in environmental remediation and water splitting: a review, Sci. Total Environ. 804 (2022) 150215, https://doi.org/10.1016/j.scitotenv.2021.150215.

[5] J. Hou, T. Zhang, T. Jiang, X. Wu, Y. Zhang, M. Tahir, A. Hussain, M. Luo, J. Zou, X. Wang, Fast preparation of oxygen vacancy-rich 2D/2D bismuth oxyhalides-reduced graphene oxide composite with improved visible-light photocatalytic properties by solvent-free grinding, J. Clean. Prod. 328 (2021) 129651, https://doi.org/10.1016/j.jclepro.2021.129651.

[6] M. Reza Gholipour, C. Dinh, F. Béland, T. Do, Nanocomposite heterojunctions as sunlight-driven photocatalysts for hydrogen production from water splitting, Nanoscale. 7 (2015) 8187–8208, https://doi.org/10.1039/C4NR07224C.

[7] F. Yuan, Y. Zheng, D. Gao, D. Meng, L. Wang, X. Hu, Relationship of structure and enhanced photocatalytic activity of S-scheme BiOCl/g-C_3N_4 heterojunction for xanthate removal under visible light, Adv. Powder Technol. 34 (2023) 104049, https://doi.org/10.1016/j.apt.2023.104049.

[8] J. Tan, J. Sin, S. Lam, H. Lin, H. Li, L. Huang, A.R. Mohamed, Fabrication of novel Z-scheme $BaFe_2O_4$/BiOCl nanocomposite with promoted visible light photocatalytic palm oil mill effluent treatment and pathogens destruction, Inorg. Chem. Commun. 152 (2023) 110659, https://doi.org/10.1016/j.inoche.2023.110659.

[9] Z. Chen, Y. Ma, W. Chen, Y. Tang, L. Li, J. Wang, Enhanced photocatalytic degradation of ciprofloxacin by heterostructured BiOCl/$Ti_3C_2T_x$ MXene nanocomposites, J. Alloys Compounds. 950 (2023) 169797, https://doi.org/10.1016/j.jallcom.2023.169797.

[10] C. Gao, G. Liu, X. Liu, X. Wang, M. Liu, Y. Chen, X. Jiang, G. Wang, Z. Teng, W. Yang, Flower-like n-Bi_2O_3/n-BiOCl heterojunction with excellent photocatalytic performance for visible light degradation of bisphenol a and methylene blue, J. Alloys Compounds. 929 (2022) 167296, https://doi.org/10.1016/j.jallcom.2022.167296.

[11] W. Hou, H. Xu, Y. Cai, Z. Zou, D. Li, D. Xia, Precisely control interface OVs concentration for enhance 0D/2D $Bi_2O_2CO_3$/BiOCl photocatalytic performance, Appl. Surf. Sci. 530 (2020) 147218, https://doi.org/10.1016/j.apsusc.2020.147218.

[12] D. Zhang, C. Su, S. Yao, H. Li, X. Pu, Y. Geng, Facile in situ chemical transformation synthesis, boosted charge separation, and increased photocatalytic activity of $BiPO_4$/BiOCl p-n heterojunction photocatalysts under simulated sunlight irradiation, J. Phys. Chem. Solids. 147 (2020) 109630, https://doi.org/10.1016/j.jpcs.2020.109630.

[13] Z. Liu, R. Liu, Y. Mu, Y. Feng, G. Dong, M. Zhang, T. Lu, In situ construction of Lead-free perovskite direct Z-scheme heterojunction $Cs_3Bi_2I_9$/Bi_2WO_6 for efficient photocatalysis of CO_2 reduction, Sol. RRL. 5 (2021) 2000691, https://doi.org/10.1002/solr.202000691.

[14] G. He, C. Xing, X. Xiao, R. Hu, X. Zuo, J. Nan, Facile synthesis of flower-like $Bi_{12}O_{17}Cl_2$/β-Bi_2O_3 composites with enhanced visible light photocatalytic performance for the degradation of 4-tert-butylphenol, Appl. Catal. B: Environ. 170–171 (2015) 1–9, https://doi.org/10.1016/j.apcatb.2015.01.015.

[15] W. Li, Z. Liu, Y. Dong, L. Wang, Z. Liu, L. Zhang, Z. Qiao, Micellar interface modulation self-assembly strategy towards mesoporous bismuth oxychloride-based materials for boosting photocatalytic pharmaceuticals degradation, Chem. Eng. J. 450 (2022) 137897, https://doi.org/10.1016/j.cej.2022.137897.

[16] A. Etogo, E. Hu, C. Zhou, Y. Zhong, Y. Hu, Z. Hong, Facile fabrication of mesoporous BiOCl/$(BiO)_2CO_3$/Bi_2O_3 ternary flower-like heterostructured microspheres with high visible-light-driven photoactivity, J. Mater. Chem. A 3 (2015) 22413–22420, https://doi.org/10.1039/C5TA06082F.

[17] Y. Peng, P. Yu, H. Zhou, A. Xu, Synthesis of BiOI/$Bi_4O_5I_2$/$Bi_2O_2CO_3$ p–n–p heterojunctions with superior photocatalytic activities, New J. Chem. 39 (2015) 8321–8328, https://doi.org/10.1039/C5NJ01662B.

[18] P. Riente, M. Fianchini, P. Llanes, M.A. Pericàs, T. Noël, Shedding light on the nature of the catalytically active species in photocatalytic reactions using Bi_2O_3 semiconductor, Nat. Commun. 12 (2021) 625, https://doi.org/10.1038/s41467-020-20882-x.

[19] C. Wang, X. Zhang, H. Qiu, W. Wang, G. Huang, J. Jiang, H. Yu, Photocatalytic degradation of bisphenol a by oxygen-rich and highly visible-light responsive $Bi_{12}O_{17}Cl_2$ nanobelts, Appl. Catal. B: Environ. 200 (2017) 659–665, https://doi.org/10.1016/j.apcatb.2016.07.054.

[20] S. Rodriguez-Mozaz, I. Vaz-Moreira, S. Varela Della Giustina, M. Llorca, D. Barceló, S. Schubert, T.U. Berendonk, I. Michael-Kordatou, D. Fatta-Kassinos, J.L. Martinez, C. Elpers, I. Henriques, T. Jaeger, T. Schwartz, E. Paulshus, K. O'Sullivan, K.M. M. Pärnänen, M. Virta, T.T. Do, F. Walsh, C.M. Manaia, Antibiotic residues in final effluents of European wastewater treatment plants and their impact on the aquatic environment, Environ. Int. 140 (2020) 105733, https://doi.org/10.1016/j.envint.2020.105733.

[21] C. Maia, C.A. Sousa, H. Sousa, F. Vale, M. Simões, Parabens removal from wastewaters by microalgae – ecotoxicity, metabolism and pathways, Chem. Eng. J. 453 (2023) 139631, https://doi.org/10.1016/j.cej.2022.139631.

[22] X. Liu, Z. Chen, W. Du, P. Liu, L. Zhang, F. Shi, Treatment of wastewater containing methyl orange dye by fluidized three dimensional electrochemical oxidation process integrated with chemical oxidation and adsorption, J. Environ. Manage. 311 (2022) 114775, https://doi.org/10.1016/j.jenvman.2022.114775.

[23] G. Zhang, L. Cai, Y. Zhang, Y. Wei, Bi^{5+}, $Bi_{(3-x)}$+, and oxygen vacancy induced BiOClxI1−x solid solution toward promoting visible-light driven photocatalytic activity, Chem. Eur. J. 24 (2018) 7434–7444, https://doi.org/10.1002/chem.201706164.

[24] L. Wang, X. Min, X. Sui, J. Chen, Y. Wang, Facile construction of novel BiOBr/$Bi_{12}O_{17}Cl_2$ heterojunction composites with enhanced photocatalytic performance, J. Colloid Interface Sci. 560 (2020) 21–33, https://doi.org/10.1016/j.jcis.2019.10.048.

[25] D. Mao, A. Yu, S. Ding, F. Wang, S. Yang, C. Sun, H. He, Y. Liu, K. Yu, One-pot synthesis of BiOCl half-shells using microemulsion droplets as templates with highly photocatalytic performance for the degradation of ciprofloxacin, Appl. Surf. Sci. 389 (2016) 742–750, https://doi.org/10.1016/j.apsusc.2016.07.178.

[26] J. Yang, T. Xie, Q. Zhu, J. Wang, L. Xu, C. Liu, Boosting the photocatalytic activity of BiOX under solar light via selective crystal facet growth, J. Mater. Chem. C. 8 (2020) 2579–2588, https://doi.org/10.1039/C9TC05752H.

[27] M. Ford-Smith, J.J. Habeeb, Kinetics of oxidation-reduction reactions between elements of groups V and VII. part I. Bismuth(V) with halide ions and other reductants, J. Chem. Soc., Dalton Trans. (1973) 461–464, https://doi.org/10.1039/DT9730000461.

[28] D. Kato, O. Tomita, R. Nelson, M.A. Kirsanova, R. Dronskowski, H. Suzuki, C. Zhong, C. Tassel, K. Ishida, Y. Matsuzaki, C.M. Brown, K. Fujita, K. Fujii, M. Yashima, Y. Kobayashi, A. Saeki, I. Oikawa, H. Takamura, R. Abe, H. Kageyama, T.E. Gorelik, A.M. Abakumov, $Bi_{12}O_{17}Cl_2$ with a sextuple Bi-O layer composed of rock-salt and fluorite units and its structural conversion through fluorination to enhance photocatalytic activity, Adv. Funct. Mater. 32 (2022) 2204112, https://doi.org/10.1002/adfm.202204112.

[29] M. Ou, F. Dong, W. Zhang, Z. Wu, Efficient visible light photocatalytic oxidation of NO in air with band-gap tailored $(BiO)_2CO_3$–BiOI solid solutions, Chem. Eng. J. 255 (2014) 650–658, https://doi.org/10.1016/j.cej.2014.06.086.

[30] W. Zhang, X. Dong, B. Jia, J. Zhong, Y. Sun, F. Dong, 2D BiOCl/$Bi_{12}O_{17}Cl_2$ nanojunction: enhanced visible light photocatalytic NO removal and in situ DRIFTS investigation, Appl. Surf. Sci. 430 (2018) 571–577, https://doi.org/10.1016/j.apsusc.2017.06.186.

[31] Z. Long, G. Xian, G. Zhang, T. Zhang, X. Li, BiOCl-$Bi_{12}O_{17}Cl_2$ nanocomposite with high visible-light photocatalytic activity prepared by an ultrasonic hydrothermal method for removing dye and pharmaceutical, Chin. J. Catal. 41 (2020) 464–473, https://doi.org/10.1016/S1872-2067(19)63474-1.

[32] S.E. Howard, F. Ruth, U.M. George, Standard X-Ray Diffraction Powder Patterns, National Bureau of Standards. 4 (1955) 54.

[33] B.Z. Nurgaliev, T.F. Vasekina, A.E. Baron, B.A. Popovkin, A.V. Novoselova, Nouveaux oxybromures et oxychlorures de bismuth, Russian Journal of Inorganic Chemistry. 28 (1983).

[34] B. Aurivillius, G. Malmros, The crystal structure of beta-Bi_2O_3, Trans. Roy. Inst. Techn. 291 (1972).

[35] S. Kong, Z. An, W. Zhang, Z. An, M. Yuan, D. Chen, Preparation of hollow flower-like microspherical β-Bi_2O_3/BiOCl heterojunction and high photocatalytic property

for tetracycline hydrochloride degradation, Nanomaterials 10 (2020), https://doi.org/10.3390/nano10010057.

[36] J. Ma, L. Shi, L. Hou, L. Yao, C. Lu, Z. Geng, Fabrication of graphene/$Bi_{12}O_{17}Cl_2$ as an effective visible-light photocatalyst, Mater. Res. Bull. 122 (2020) 110690, https://doi.org/10.1016/j.materresbull.2019.110690.

[37] V. Vivier, A. Régis, G. Sagon, J. Nedelec, L.T. Yu, C. Cachet-Vivier, Cyclic voltammetry study of bismuth oxide Bi_2O_3 powder by means of a cavity microelectrode coupled with raman microspectrometry, Electrochim. Acta. 46 (2001) 907–914, https://doi.org/10.1016/S0013-4686(00)00677-0.

[38] V. Vivier, C. Cachet-Vivier, S. Mezaille, B.L. Wu, C.S. Cha, J. Nedelec, M. Fedoroff, D. Michel, L.T. Yu, Electrochemical study of Bi_2O_3 and $Bi_2O_2CO_3$ by means of a cavity microelectrode. I. observed phenomena and direct analysis of results, J. Electrochem. Soc. 147 (2000) 4252, https://doi.org/10.1149/1.1394049.

[39] D. Lin, H. Zhang, X. An, L. Chang, A. Alameen, S. Ding, X. Du, X. Hao, Theoretical calculation assisted materials screening of BiOX (X = F, Cl, Br, I) for electrochemical absorption of cesium ions, Phys. Chem. Chem. Phys. 23 (2021) 8500–8507, https://doi.org/10.1039/D0CP06195F.

[40] N. Vladislavic, S. Brinic, Z. Grubac, M. Buzuk, Study of bi film formation on different carbon based electrodes for possible applicability in electroanalytical determination of cysteine, Int. J. Electrochem. Sci. 9 (2014) 6020–6032, https://doi.org/10.1016/S1452-3981(23)10866-2.

[41] M.R.d.S. Pelissari, L. Pereira Camargo, F.M.L. Pontes, L.H. Dall'Antonia, Synthesis and deposition of bismuth oxychloride with a rose-type flower shape and photoelectroactivity evaluation in the methyl orange discoloration reaction, Coloration Technology. 139 (2023) 742–757, https://doi.org/10.1111/cote.12685.

[42] A. Navalón, O. Ballesteros, R. Blanc, J.L. Vílchez, Determination of ciprofloxacin in human urine and serum samples by solid-phase spectrofluorimetry, Talanta 52 (2000) 845–852, https://doi.org/10.1016/S0039-9140(00)00437-9.

[43] X. Van Doorslaer, J. Dewulf, H. Van Langenhove, K. Demeestere, Fluoroquinolone antibiotics: an emerging class of environmental micropollutants, Sci. Total Environ. 500–501 (2014) 250–269, https://doi.org/10.1016/j.scitotenv.2014.08.075.

[44] D. Błędzka, J. Gromadzińska, W. Wąsowicz Parabens, From environmental studies to human health, Environ. Int. 67 (2014) 27–42, https://doi.org/10.1016/j.envint.2014.02.007.

[45] E. Hager, J. Chen, L. Zhao, Minireview: parabens exposure and breast cancer, international journal of environmental research and public, Health. 19 (2022), https://doi.org/10.3390/ijerph19031873.

[46] P. Arabkhani, A. Asfaram, Development of a novel three-dimensional magnetic polymer aerogel as an efficient adsorbent for malachite green removal, J. Hazard. Mater. 384 (2020) 121394, https://doi.org/10.1016/j.jhazmat.2019.121394.

[47] T. Senasu, S. Nijpanich, S. Juabrum, N. Chanlek, S. Nanan, CdS/BiOBr heterojunction photocatalyst with high performance for solar-light-driven degradation of ciprofloxacin and norfloxacin antibiotics, Appl. Surf. Sci. 567 (2021) 150850, https://doi.org/10.1016/j.apsusc.2021.150850.

[48] T. Ahamad, M. Naushad, S.M. Alshehri, Analysis of degradation pathways and intermediates products for ciprofloxacin using a highly porous photocatalyst, Chem. Eng. J. 417 (2021) 127969, https://doi.org/10.1016/j.cej.2020.127969.

[49] Z. He, H. Yang, J. Su, Y. Xia, X. Fu, L. Wang, L. Kang, Construction of multifunctional dual Z-scheme composites with enhanced photocatalytic activities for degradation of ciprofloxacin, Fuel 294 (2021) 120399, https://doi.org/10.1016/j.fuel.2021.120399.

[50] K. Mogolodi Dimpe, P.N. Nomngongo, Application of activated carbon-decorated polyacrylonitrile nanofibers as an adsorbent in dispersive solid-phase extraction of fluoroquinolones from wastewater, J. Pharma. Anal. 9 (2019) 117–126, https://doi.org/10.1016/j.jpha.2019.01.003.

[51] T. Angelov, A. Vlasenko, W. Tashkov, HPLC determination of pKa of parabens and investigation on their lipophilicity parameters, J. Liq. Chromatogr. Rel. Technol. 31 (2007) 188–197, https://doi.org/10.1080/10826070701738787.

[52] F. Guo, J. Chen, J. Zhao, Z. Chen, D. Xia, Z. Zhan, Q. Wang, Z-scheme heterojunction g-C_3N_4@PDA/BiOBr with biomimetic polydopamine as electron transfer mediators for enhanced visible-light driven degradation of sulfamethoxazole, Chem. Eng. J. 386 (2020) 124014, https://doi.org/10.1016/j.cej.2020.124014.

[53] X. Xiao, M. Lu, J. Nan, X. Zuo, W. Zhang, S. Liu, S. Wang, Rapid microwave synthesis of I-doped $Bi_4O_5Br_2$ with significantly enhanced visible-light photocatalysis for degradation of multiple parabens, Appl. Catal. B: Environ. 218 (2017) 398–408, https://doi.org/10.1016/j.apcatb.2017.06.074.

[54] X. Xiao, R. Hu, S. Tu, C. Zheng, H. Zhong, X. Zuo, J. Nan, One-pot synthesis of micro/nano structured β-Bi_2O_3 with tunable morphology for highly efficient photocatalytic degradation of methylparaben under visible-light irradiation, RSC Adv. 5 (2015) 38373–38381, https://doi.org/10.1039/C5RA03200H.

[55] O. Tomita, B. Ohtani, R. Abe, Highly selective phenol production from benzene on a platinum-loaded tungsten oxide photocatalyst with water and molecular oxygen: selective oxidation of water by holes for generating hydroxyl radical as the predominant source of the hydroxyl group, Catal Sci. Technol. 4 (2014) 3850–3860, https://doi.org/10.1039/C4CY00445K.

[56] J. Guo, H. Sun, X. Yuan, L. Jiang, Z. Wu, H. Yu, N. Tang, M. Yu, M. Yan, J. Liang, Photocatalytic degradation of persistent organic pollutants by Co-Cl bond reinforced CoAl-LDH/$Bi_{12}O_{17}Cl_2$ photocatalyst: mechanism and application prospect evaluation, Water Res. 219 (2022) 118558, https://doi.org/10.1016/j.watres.2022.118558.

[57] X. Hu, X. Hu, Q. Peng, L. Zhou, X. Tan, L. Jiang, C. Tang, H. Wang, S. Liu, Y. Wang, Z. Ning, Mechanisms underlying the photocatalytic degradation pathway of ciprofloxacin with heterogeneous TiO_2, Chem. Eng. J. 380 (2020) 122366, https://doi.org/10.1016/j.cej.2019.122366.

[58] L. Sruthi, B. Janani, S. Sudheer Khan, Ibuprofen removal from aqueous solution via light-harvesting photocatalysis by nano-heterojunctions: A review, Separation and Purification Technology. 279 (2021) 119709. 10.1016/j.seppur.2021.119709.